3-24-2016

Design and Analysis of a Retroreflective Array for IR Application

Michael E. Bollinger

DESIGN AND ANALYSIS OF A RETROREFLECTIVE ARRAY FOR IR APPLICATION

THESIS

Michael E. Bollinger, Captain, USAF

AFIT-ENG-MS-16-M-005

DEPARTMENT OF THE AIR FORCE
AIR UNIVERSITY

AIR FORCE INSTITUTE OF TECHNOLOGY

Wright-Patterson Air Force Base, Ohio

AFIT-ENG-MS-16-M-005

DESIGN AND ANALYSIS OF A RETROREFLECTIVE ARRAY FOR IR APPLICATION

THESIS

Presented to the Faculty

Department of Electrical and Computer Engineering

Graduate School of Engineering and Management

Air Force Institute of Technology

Air University

Air Education and Training Command

In Partial Fulfillment of the Requirements for the

Degree of Master of Science in Electrical Engineering

Michael E. Bollinger, B.S.

Captain, USAF

March 2016

AFIT-ENG-MS-16-M-005

DESIGN AND ANALYSIS OF A RETROREFLECTIVE ARRAY FOR IR APPLICATION

Michael E. Bollinger, BS
Captain, USAF

Committee Membership:

Maj Michael D. Seal, PhD
Chair

Lt Col Jeremy Stringer, PhD
Member

Michael A. Marciniak, PhD
Member

Abstract

This research investigates the adaptation of a Van Atta style of retrodirective array designed to work at 2 GHz to work in the infrared spectrum of 8-12 μm centered at 30 THz. The Computational Research and Engineering Acquisition Tools and Environments (CREATE) software suite and high performance computing (HPC) resources of the HPC Modernization program were utilized to model and simulate multiple steps of an adaptation process to illustrate and examine the incremental performance changes of frequency scaling the design. Two different substrate materials, germanium and hafnium oxide, are evaluated as the dielectric materials, and a comparison of the broadband performance of scaled designs using both dielectric materials shows that hafnium oxide provides better performance than germanium for this application. In addition, both gold and aluminum are evaluated for use in scaled designs. The results suggest that the cost savings and oxide bonding benefits of aluminum outweigh the slight performance advantage of gold. The Van Atta array concept is adaptable to IR wavelengths and microfabrication. Improved final broadband performance of the scaled design is a factor of approximately three and a half better than the 2 GHz design.

Acknowledgments

I would like to express my sincere appreciation to my research advisor, Maj Michael D. Seal, for his guidance and support throughout the course of this thesis effort. I appreciated his patience, guidance, support, and insight during the course of work required to produce this thesis.

Michael E. Bollinger

Table of Contents

List of Figures

Figure Page

List of Tables

List of Abbreviations

CREATE	Computational Research and Engineering Acquisition Tools and Environments 3
EM	Electromagnetic 1
Ge	Germanium 2
GHz	Gigahertz 1
HfO_2	Hafnium oxide 2
HPC	High performance computing 3
IR	Infrared 1
LO	Local oscillator 7
MHz	Megahertz 14
PEC	Perfect electrical conductor 21
RAM	Random access memory 20
RCS	Radar cross section 34
RF	Radio frequency 8
THz	Terahertz 1
UV	Ultraviolet 17

DESIGN AND ANALYSIS OF A RETROREFLECTIVE ARRAY FOR IR APPLICATION

I. Introduction

General Issue

In complex optical trains, baffles limit the visible wavelength light arriving at a detector to only the light coming in near the optical axis, preventing reflected light from the sides of the apparatus from arriving on the sensor. This type of absorptive baffle is not effective in the long-wave-infrared (IR) spectrum, as it would actually increase the amount of area providing self-emission in the IR spectrum observed by the sensor and degrade the sensor's performance. The use of a passive retrodirective engineered surface coating on baffles could reduce scattered energy while presenting the detector only a reflection of itself. Even in an uncooled system, the sensor is the coldest point in the optical train. Reducing the overall extraneous IR signals arriving at the sensor will improve sensitivity.

The Van Atta array is a well-documented and accepted passive retro reflective design in the gigahertz (GHz) range [1, 2]. This type of symmetrical design is desirable to allow a large array to be created efficiently [3] which is strictly necessary for IR applications. The design prescribed by Christodoulou and Chrissoulidis [3] for operation centered at 2 GHz serves as a suitable baseline to explore the application of Van Atta arrays at the terahertz (THz) frequencies of the long-wave-IR portion of the electromagnetic (EM) spectrum.

Problem Statement

Scaling the Van Atta retro reflective array concept to be effective in the long-wave-IR wavelengths, 8-12 μm, requires more than just making the design smaller. Adjusting for the behavior of the dielectrics, the difference in the way sputtered metals behave versus bulk metals, and fabrication limitations for nanometer scale features are all required. In the THz range, the normal visible wavelength silicon dielectric is ineffective due to its high losses, so other dielectric materials are examined, each with their own properties that must be taken into consideration in the design of the array [4, 5]. The two dielectric materials considered in this thesis are germanium (Ge) and hafnium oxide (HfO_2). Besides availability and general suitability for microfabrication processes, germanium and hafnium oxide are chosen specifically to examine areas of advantages and disadvantages. Ge has a high relative permittivity, which greatly reduces the size of the individual patches that make up the array, and can potentially improve broadband performance [6]. HfO_2 has a lower relative permittivity in the IR but is also frequency dispersive in the THz regime, which will greatly affect the performance of any final design; however, the lower relative permittivity will increase the patch coverage of the design.

The inherent limitations associated with microfabrication also must be taken into consideration, such as the type of process to be used in fabrication and the minimum feature size capable of being formed by the process chosen [7]. The minimum metal layer thickness required for the design's elements is dependent on the microfabrication process, but also on the skin effect to achieve good conductivity. A layer thickness that is 4-5 times the skin effect depth achieves good conductivity [8].

Modification of the baseline design is required to take into consideration the fabrication limitations, the materials used, and the element sizes needed for IR scale operation. The simulation and assessment of the design will provide predicted performance data and help determine if the design merits fabrication and further testing.

Methodology

In order to show the progression and relate all results back to the original design's performance [3], the original design is modeled in Capstone and simulated in SENTRi, which are both part of the Computational Research and Engineering Acquisition Tools and Environments (CREATE) software development program. Capstone is computer-drafting software capable of producing surface and volume meshes. A variety of simulation software use the exported meshes to analyze design performance. SENTRi is an example of a general computational electromagnetic software tool with a wide range of RF applications and employs a composite finite element and boundary integral method technique to solve closed and open scattering problems [9, 10].

Solution convergence is established by conducting multiple runs on a local large memory system in order to show that the result from the high-performance computing (HPC) system is meaningful and set bounds on its expected errors. Each run on the local system has a higher-fidelity mesh. The results of which, showing the convergence of the solution and allow a comparison between different results from different fidelity meshes.

To allow for a meaningful comparison between the 2-GHz and 30-THz designs, a frequency and area normalized scattering metric is defined. Assessing the differences in the results between the Van Atta array designs and a flat plate of the same size creates the

normalized metric. The normalized scattering metric allows performance comparisons across physical size and wavelength scales. The implementation of sequential modifications of the original design, to reflect microfabrication methods imposed changes, allows an assessment of each step while maintaining traceability to the original.

Each design change is modeled and simulated to assess the effect these changes have on the normalized performance of the design. Changing the form of the trace bends to a stepped corner is required since angled traces with filet corners (Figure 1), which are the best choice from a design standpoint [11], are not viable in microfabrication. The published design [3] used impedance-matching transformers (Figure 2) that were a quarter of the guided wavelength long. The purpose of these transformers was to transition from the 50Ω impedance of the microstrip traces to the approximate 377Ω impedance of the patches. These transformers had to be removed since their implementation is not possible at the IR scale. The third design adjustment's performance is compared to the first and second results to assess the progression of performance change. Scaling the fabrication comparable design to the nanometer scale creates a design concept applicable to two different dielectric material substrates. Comparing the two resulting nanometer scale designs to the baselines and to each other allows an assessment of which design exhibits the best performance for its design tradeoffs. Further modifying the most promising substrate design to try to improve performance parameters such as bandwidth and retro return is the final modification step.

Figure 1. Examples of three common corner forms used in microstrip traces showing progressively worse performance, from left to right, are the filet, step, and right angle corners [11]**.**

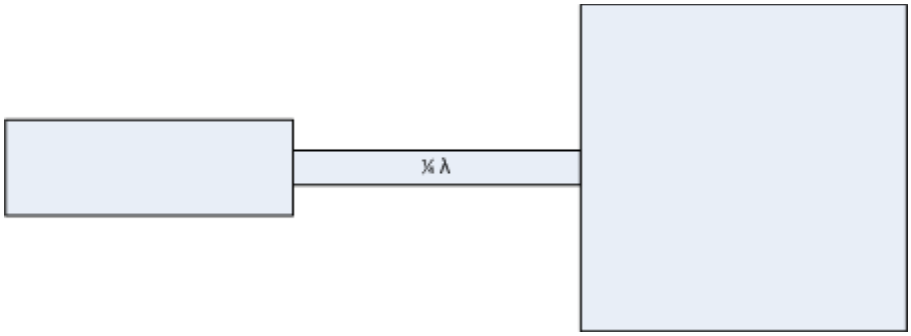

Figure 2. A visual representation of a quarter-wavelength impedance matching transformer used to match the impedance of the patch to the microstrip.

Implications/Applications

With an effective design, the application in optical trains to improve IR sensitivity provides an alternative technology concept for uncooled IR sensor devices, with complex optical trains, which provides better performance by reducing extraneous signals arriving at the sensor. The results also lead to better understanding of the effects of miniaturization of a family of planar antenna designs to be effective in the IR range.

Document Organization

Chapter II provides a general review and background on the key topics discussed along with a discussion of relevant past works upon which this thesis builds. Chapter III describes in detail the methodology used in designing and simulating the various designs to determine the viability of the nanometer scale retro reflective array. Chapter IV presents the results of the comparisons, a discussion of the best design, and an analysis of what characteristics produced the best results. Chapter V summarizes the findings of the thesis and presents recommendations for future research opportunities to continue the work started here. Appendix A contains graphical representations of simulation results for each design examined.

II. Literature Review

Theoretical Background

Retrodirective arrays have the characteristic of reflecting an incident wave toward the source direction without any prior knowledge of, or information about, the incoming signal location. Conventional solutions for this function are phased-array antennas that steer their beams by exciting elements with phase shifters. Retrodirective arrays steer their beams automatically without any intensive algorithms or phase shifters in response to an interrogating signal. The formation of the retrodirective beam is limited in that the beam is directed only toward the source radiator; however, it achieves retrodirective behavior with no knowledge of the source location [12]. Since this research specifically focuses on the ability to passively send the signal received back to the source of the signal, the retrodirective array is an ideal choice to investigate for this function.

In "Retrodirective Array Technology", [12] three different retrodirective architectures were examined including the corner reflector, the Van Atta array, and the heterodyne phase conjugating array. The advantages and disadvantages of these architectures were presented, and are summarized here. The corner reflector consists of orthogonal metal sheets. However, the corner reflector metal sheets are large with respect to wavelength in order to minimize the effects of edge diffraction [12]. As the corner reflector has been previously investigated in the IR range [13], this research focuses specifically on electrically small planar structures. The heterodyne phase conjugating architecture reverses its phase gradient and uses a mixer at each antenna element that mixes the signal received at the antenna with the feed from a local oscillator (LO), with

double the frequency of the incident wave. The heterodyne mixing causes the incoming radio frequency (RF) signal at each element to mix with a LO as shown in Figure 3 [12].

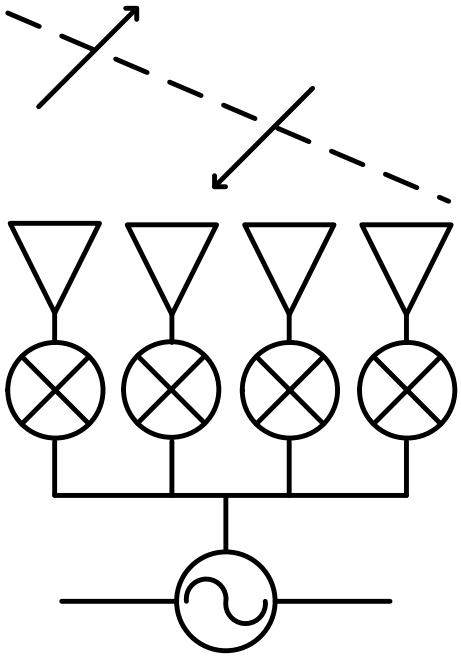

Figure 3. The phase conjugation array uses mixers and a local oscillator to achieve phase reversal of incoming wave with heterodyne mixing of the incoming signal [12] **.**

The phase conjugation retrodirective array has the advantage of the array elements being arbitrarily located, not necessarily with equal inter-element spacing, nor existing in the same plane; thus, it can easily conform to an object's surface. Another advantage is that by changing the LO frequency, the reradiated wave can be readily frequency-modulated [12]. However, the phase conjugation array requires a mixer circuit with a large-frequency difference between the RF and LO signals for each array element, a LO operating at twice the system frequency, and a corresponding distribution network from the LO to the entire array of elements. These requirements may make the array complicated, bulky, costly, and, most importantly, are barriers to frequency scaling in the THz range.

The Van Atta array consists of pairs of antenna elements equally spaced from the array center with transmission lines of equal length or, if equal lengths are not possible, the difference in lengths are multiples of the guided wavelength [12]. The arrangement of the array causes a reversal, positive to negative or negative to positive, of the phase progression for the outgoing signal, causing the array arrangement to retro-reflect back in the same direction. As shown in Figure 4, every antenna serves as both a receiving and a transmitting antenna. The signal received by one antenna is reradiated by the antenna connected by the transmission line, causing the phase order to be transposed from the incoming signal across the center of the array. Provided the array is linear and the lines are of equal length, the reradiated signal will have the opposite phase of the incident signal and will be radiated back in the direction from which the signal was received [12].

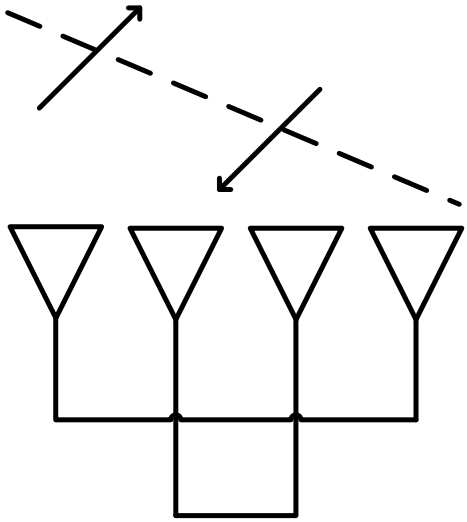

Figure 4. A passive Van Atta array achieves phase reversal by each antenna reradiating the signal received by the connected antenna through equal length transmission lines [12]**.**

The Van Atta array is capable, in principle, of reflecting a wave incident at any angle, but its performance is limited in practice by the directivity of the radiators [12].

Since the lengths of the connecting transmission lines are equal, the most frequency-dependent components in the Van Atta array are the antenna elements. The geometrical arrangement of the Van Atta array is restricted to planar wavefronts and topologies and is spatially inefficient for realizing retrodirectivity on many applications [12]. However, the research conducted here specifically focuses on planar topologies. The passive and simplistic nature of the Van Atta array make it the most promising retrodirective array to further develop for planar IR devices.

Dr. L. C. Van Atta patented the Van Atta array in 1959 [13]. A four-by-four array of dipole antennas was studied in a paper by Sharp and Diab [2]. Sharp and Diab compared the performance of the Van Atta array against the performance of a flat plate of the same aperture area. The result of the experiment was that the Van Atta array compared favorably with the corner reflector, which therefore established the Van Atta array as a viable retrodirective array. Sharp and Diab also suggested that the Van Atta array could be made to reflect a wave of any polarization by arranging half of the radiators to be vertically polarized and the other half to be horizontally polarized, or by using all circularly polarized radiators. With 50 years of history and development behind the Van Atta array, there are numerous papers that have considered multiple applications of the Van Atta array using different antennae types designed to perform at different frequencies [1–3, 13, 14]. The application intended in this research requires a very small profile and operation centered around $10\,\mu m$ or 30 THz. While the concept is sound and well vetted, the challenges of massive frequency scaling from the GHz range to the THz have yet to be addressed.

Van Atta Array Design Review

Nair and Fusco [1] described a design using square patch antennas arranged in the Van Atta array design. In this design, paired patches were connected on orthogonal sides, to allow both horizontal and vertical polarized waves to be retroreflected [1]. To accommodate the requirement that the Van Atta array maintain interconnecting transmission lines of equal length, the interior lines are meandered, as shown in Figure 5. Comparing the design to a metal plate showed an improved retrodirective action angle from 24° for a flat plate to 50° for the Van Atta design. This design demonstrated the effectiveness of microstrip patch antennas and microstrip lines used in a Van Atta design. However, the meander design used to interconnect the patches and the feeding from the same side as the paired patch caused an asymmetric design incompatible with large arrays.

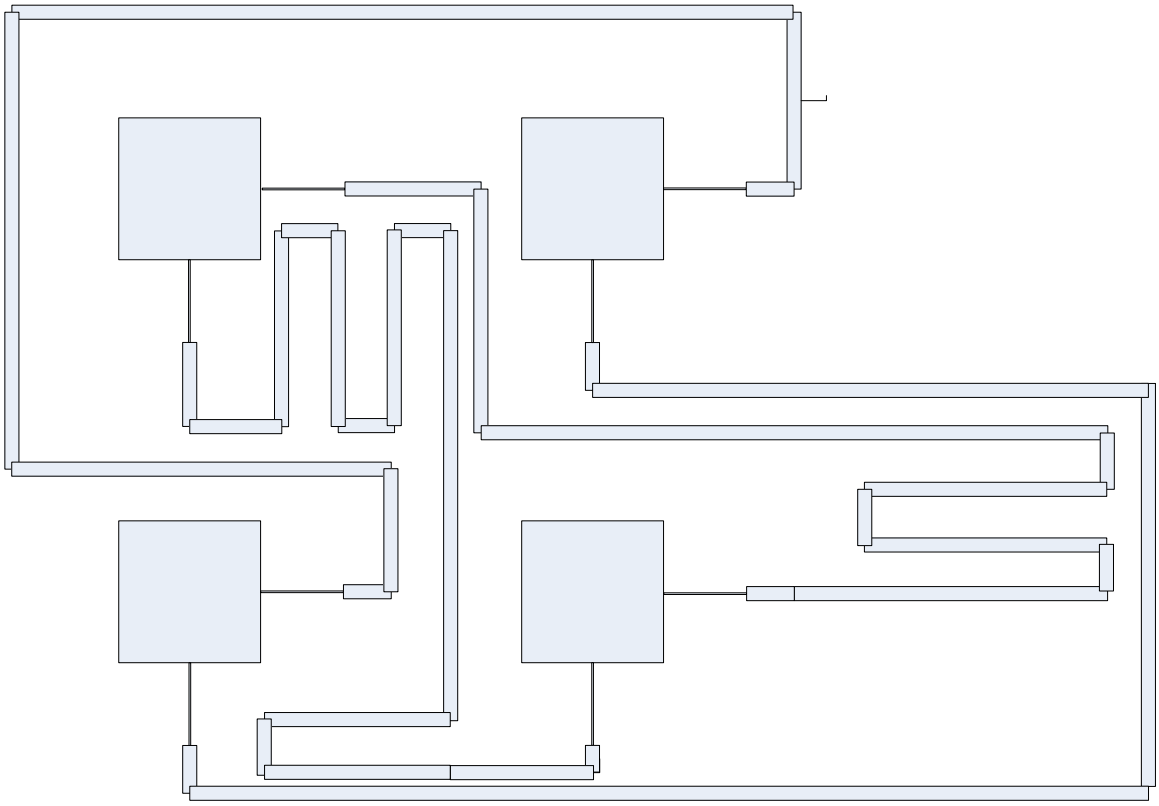

Figure 5. Example of meandered trace linesto accommodate all trace lines being of equal length and feeding into the corresponding side of the paired patch antenna.

Christodoulou and Chrissoulidis [3] also used two-port square microstrip patches to achieve a dual-polarized design. The advantage of this design is the physical and polarimetrically symmetric approach, shown in Figure 6, allowing the creation of effective arrays from multiple instances of the design. The patches were not connected on the same sides, which required a difference in the transmission lines of half of the guided wavelength to be included in the transmission line design. Another consequence of the feed side of the patches was that the retrodirective wave was a cross-polarized wave instead of a co-polarized wave. As proposed by Christodoulou and Chrissoulidis, the interior transmission lines do not follow the right angle paths, best suited to microfabrication processes, but this was not an original design requirement and will be

addressed in this work. Christodoulou and Chrissoulidis' design included quarter wavelength transformers to provide impedance matching at the designed operating frequency between the patches and transmission lines [3]. Accounting for this in the design process of frequency scaling to operate in the THz range is required. Christodoulou and Chrissoulidis' design was intended to operate at 2 GHz. Using this design as a basis allows the creation of a baseline to compare performance of the designs as changes are made to accommodate microfabrication limitations and scaling the design to operate in the long-wave-IR region of the EM spectrum centered at $10\,\mu\text{m}$ (30 THz).

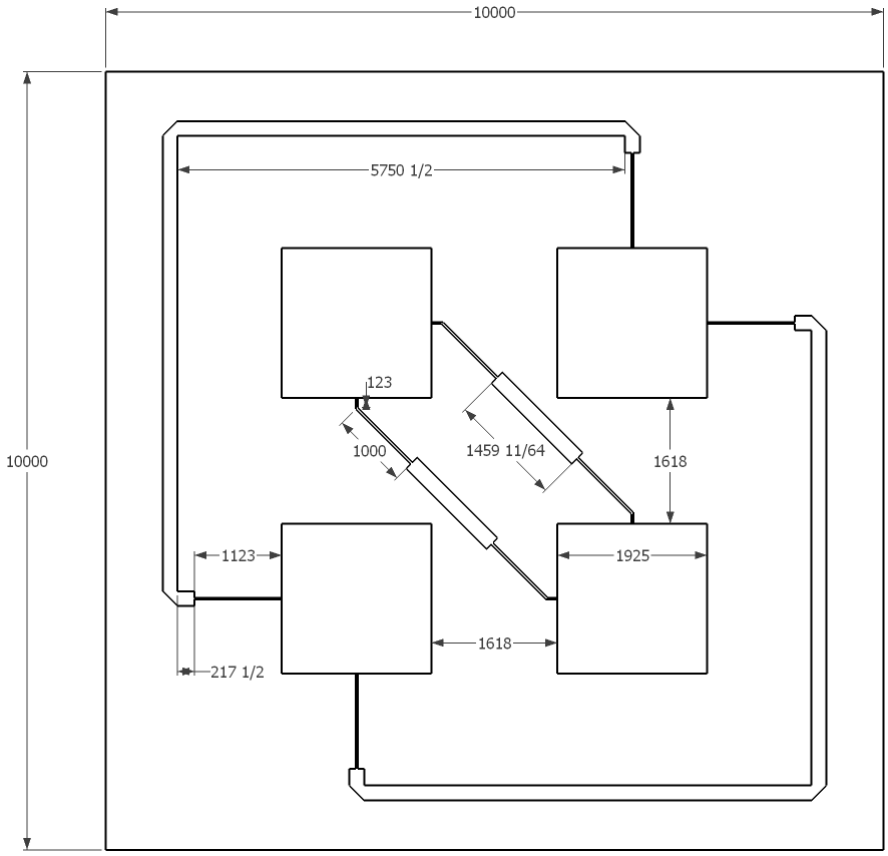

Figure 6. The 2D patch retrodirective antenna design published by Christodoulou and Chrissoulidis has angled transmission lines, filet corners, and 2.5λ difference between interior traces and external traces [3]. All units are in mils.

There are three key points drawn from the published design shown in Figure 6, which will form the basis of the research design. First, the 0.6 free space wavelength spacing between the centers of each patch antenna mitigates antenna mutual coupling. Second, the 2.5 guided wavelength difference in the lengths of the interconnecting microstrip lines, which takes into account the different feed sides. Third, the one-half dielectric wavelength sizing of the patches allows for proper operation centered on a specific frequency. Micro-patch antennas, microstrip transmission lines, microfabrication limitations, and effective wavelength are necessary design background topics to be reviewed in order to explain the changes required to the baseline design for long-wave-IR operation.

Design Background

Carver and Mink [16] described the analytical and experimental design approaches for microstrip antenna element design. The microstrip is described as a sandwich of two parallel conducting layers separated by a single thin dielectric substrate, as shown in Figure 7. The lower conductor functions as a ground plane, and the upper conductor functions as the antenna. Practical microstrip antennas had been previously developed for use from 400 megahertz (MHz) to 38 GHz with expectation to exceed 60 GHz [16].

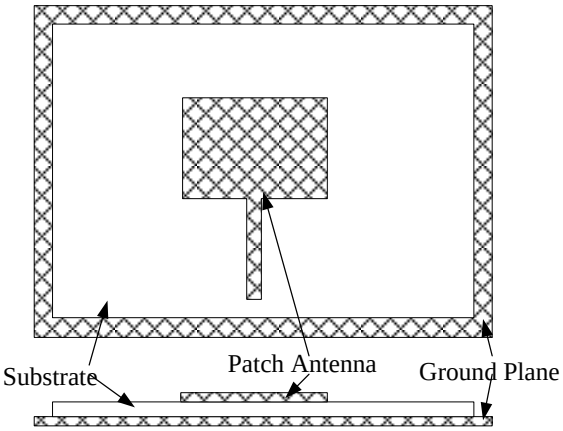

Figure 7. A rectangular patch antenna example showing the separation of the antenna and traces from the ground plane by the dielectric substrate and how the transmission line feeds into a patch antenna [16]**.**

The microstrip antenna performance is highly dependent upon the relative permittivity of the substrate used in the design. The change in operating frequency of a thin substrate microstrip antenna, as a function of the change in relative permittivity, showed that in order to have a ± 0.5 percent accuracy in the frequency, the required accuracy in the relative permittivity of the substrate material would need to be ± 0.025. Thus, the selection of the substrate material is a key concern when designing microstrip antennas [16].

Microstrip line design, as described in "Advanced Electromagnetic Theory" [17], introduced the concept of using an approximate design process, expressed in a series of equations. The size of the square patch antenna is determined from the guided wavelength, λ_g, which can found from Equation (1), where λ_0 is the wavelength in free space, and ε_r is the relative permittivity of the separating material. The size of the patch is half the dielectric wavelength. As the patch is moved closer to the ground plane, less energy is radiated and more energy is stored in electric fields due to the capacitance and

inductance of the patch. A rule-of-thumb equation for frequency bandwidth response is shown in Equation (2) [19], where d is the height of the patch above the ground plane, W is the width of the patch, Z_0 is the impedance of free space, and R_{rad} is the radiation resistance of the antenna. Impedance of free space is approximately $377\,\Omega$, and typical radiation resistance is $150\ \Omega$, which leads to equation(3).

$$\lambda_d = \frac{\lambda_0}{\sqrt{\varepsilon_r}} \tag{1}$$

$$\frac{\delta f}{f_{res}} = \frac{Z_0}{2R_{rad}} \frac{d}{W} \tag{2}$$

$$\frac{\delta f}{f_{res}} = 1.2 \frac{d}{W} \tag{3}$$

Choosing a dielectric substrate material and desired bandwidth leads to the required height of the substrate over the ground plane utilizing Equations (1), (2), and (3). Once the height of the dielectric and required width of the patch antenna have been determined, the size of the microstrip lines used to connect the patches can then be found from the desired line impedance, typically $Z_0 = 50\Omega$, and the relative permittivity of the intended dielectric material. Solving the equations given by Balanis for $W_{eff} < h$, shown in Equations (4) and (5), where t is the thickness of the traces and h is the height of the substrate that separates the traces from the ground plane, yields the required effective width. The actual required width can be found from Equation (6), once a dielectric substrate height has been set. The minimum thickness of the microstrip line and patches is limited by microfabrication methods [8, 18, 19].

$$\varepsilon_{eff} = \frac{\varepsilon_r + 1}{2} + \frac{\varepsilon_r - 1}{2}\left[\left(1 + 12\left(\frac{h}{W_{eff}}\right)\right)^{-1/2} + 0.04\left(1 - \left(\frac{W_{eff}}{h}\right)\right)^2\right] \quad (4)$$

$$Z_0 = \frac{60}{\sqrt{\varepsilon_{eff}}} \ln\left(8\frac{h}{W_{eff}} + 0.25\frac{W_{eff}}{h}\right)\Omega \quad (5)$$

$$W_{eff} = W + \left(\frac{1.25}{\pi}\right) \times t \times \left(1 + \ln\left(\frac{2h}{t}\right)\right) \quad (6)$$

Broers presented some of the limitations imposed by microfabrication methods in a 1986 Clifford Paterson lecture [21]. Thin-film microfabrication is commonly used in semiconductor integrated circuits and is a proven method of creating circuit designs much more complicated than simple Van Atta array patch antenna designs. There are different methods for thin-film microfabrication. The overlay method is limited by the resolution of the resist pattern. In the case of the highest-resolution resists, resolution is not set by the resist itself but by the resolution of the exposing tool [21].

Another method, presented by Broers [21], that avoids the use of resists makes use of sharp steps on surfaces, as seen in Figure 8, which is limited by the sharpness of the step and the ability to control the thickness of the deposited film. Utilizing sharp surface steps can produce structures smaller than 0.1 micrometer (μm), but the pattern shapes that can be formed are limited. Ultraviolet (UV) shadow printing has a high resolution, but it can cause defects if the mask and wafer accidently touch. Ultimately, linewidth is limited by the thickness of the imaging layer, and 250 nm dimensions in 100-nm-thick resist are possible. X-ray lithography uses a process similar to UV shadow printing but has a possibly higher resolution, due to the shorter wavelengths of X-rays versus UV light. X-ray lithography offers sharper exposure distributions in thick resist

layers, except for dimensions of less than 100 nm, where electrons produce higher ratios of resist thickness to minimum linewidth. In summary, X-ray lithography is the most promising method for producing devices smaller than 750 nm, due to cost compared to electron beams and process margins compared with other optics [22]. However, ruling out direct-write electron beam lithography is not possible due to the ability to shape complex features at small scales, but a cost to benefit analysis would be required.

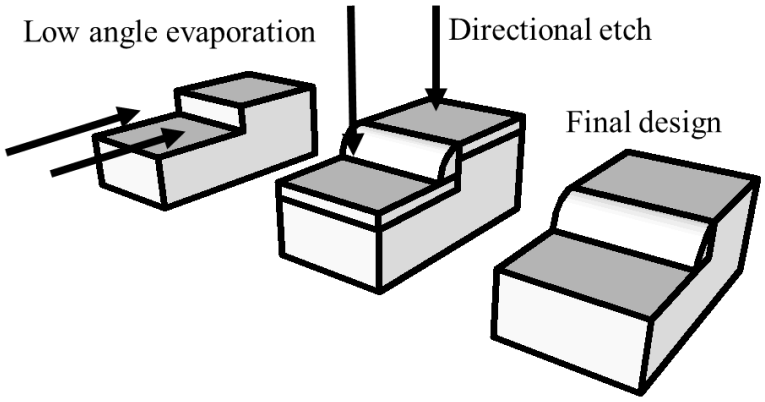

Figure 8. Fabrication example of using steps to make features in microfabrication [22]**.**

Some newer technological developments could allow for more precise feature development [22]. The Nanoscribe photonic professional laser lithography system is an example of taking the idea of 3D printers to allow for micro- and nano-printing and is touted as the next generation of laser lithography. Nanoimprint lithography has been shown to create feature sizes about 45 nm [24]. However, in this research, established techniques will be explored as microfabrication options.

Metamaterial design applications in the IR range have been explored and established fabrication techniques that are applicable in the THz range of the EM

spectrum [25]. Soukoulis published multiple articles on the results of taking an RF split ring resonator and scaling it to work in the THz scale. One issue discovered was that the metal starts to strongly deviate from an ideal conductor at high frequencies [26–28]. Having established fabrication techniques and designs allows for confidence in scaling a 2-GHz design to operate at 30 THz.

The trace corner choices available are varied and have been thoroughly explored and tested [11]. While the best choice would be to implement the filet corner on the traces, limiting the design to the right angle capabilities [7] restricts the options. The 0.70 trace width notch corner, illustrated in Figure 1, is considered a fair to good trace corner design [11] and would be simplest to implement in this design. The half trace width double notch design [11] was not chosen due to the precision required at already small scales that would be needed to accurately implement the double notches.

Summary

The Van Atta array is the best choice for this research, amongst the retrodirective array options considered, due to the passive nature of the design and the planar topology the design utilized. The published design [3] being used as a baseline provides the symmetry and performance against which the scaled design can be effectively compared. The initial modifications required to reduce the design's size and to accommodate the limitations of microfabrication were identified and explained. Well established research in both microfabrication techniques and patch antenna design form the basis for scaling the 2-GHz design presented into a design effective in the long-wave-IR region of the EM spectrum.

III. Methodology

Introduction

The design of a retrodirective Van Atta array capable of working in the IR range of $8-12\mu m$ requires several incremental steps to be taken and examined to ensure a viable result is obtained. First, the solutions obtained from HPC resources with limited random access memory (RAM) must be shown to be viable by performing a solution convergence test on a local high-memory workstation. Next, a simulation of the original 2-GHz design by Christodoulou and Chrissoulidis [3] must be completed to allow comparisons of incremental results to the results previously published. An examination of the performance changes due to each incremental modification of the published design to allow for microfabrication limitations and THz operation must be completed, to identify how each step affects broadband retrodirective performance. A comparison of the performance of the two substrate choices is required to determine which substrate will be used for further design refinement. Examining the difference between the performance of gold and aluminum traces allows a final design to be chosen which has the best broadband retrodirective performance and is cost effective. The optimal choice will undergo further analysis and refinement to show performance and promise of further development.

Solution Convergence Testing

Making use of the available HPC resources to run SENTRi simulations allows more simulations to run in a shorter period of time than would be possible on local machines. However, the 30 GB of node memory available on HPC resources sets a

limitation on how fine a mesh can be used in the model. This directly affects solution accuracy.

Solution convergence is desired to indicate that a solution from the model is viable. Convergence may be shown by modeling progressively finer meshes, until the limit of HPC available memory is reached. Further mesh refinement is continued on local high-memory workstations to allow the solution error to be estimated. The mesh is refined until the limits of the local high-memory workstations are reached, or when the mesh becomes so fine that low frequency breakdown occurs. The initial design by Christodoulou and Chrissoulidis [3] is used as a baseline for the solution convergence test, since the solution can be compared to previous results.

Christodoulou and Chrissoulidis' Design Simulation and Performance Metrics

The design by Christodoulou and Chrissoulidis is implemented in simulation to show that the CREATE-RF suite of applications is capable of reproducing similar results to those published [3]. Figure 9 shows the design implemented to reproduce Christodoulou and Chrissoulidis' work. Using the same size substrate as the modeled design, a flat plate design is also implemented to evaluate the performance improvement of the Van Atta design over a flat plate. Both designs are modeled using infinitely thin perfect electrical conductor (PEC) patches and traces. The results from the CREATE-RF suite at 2-GHz are compared to the original published results [3] providing validation of the SENTRi output. To provide a comparison baseline, the broadband performance of the design by Christodoulou and Chrissoulidis is also examined and normalized versus a flat plate of the same size.

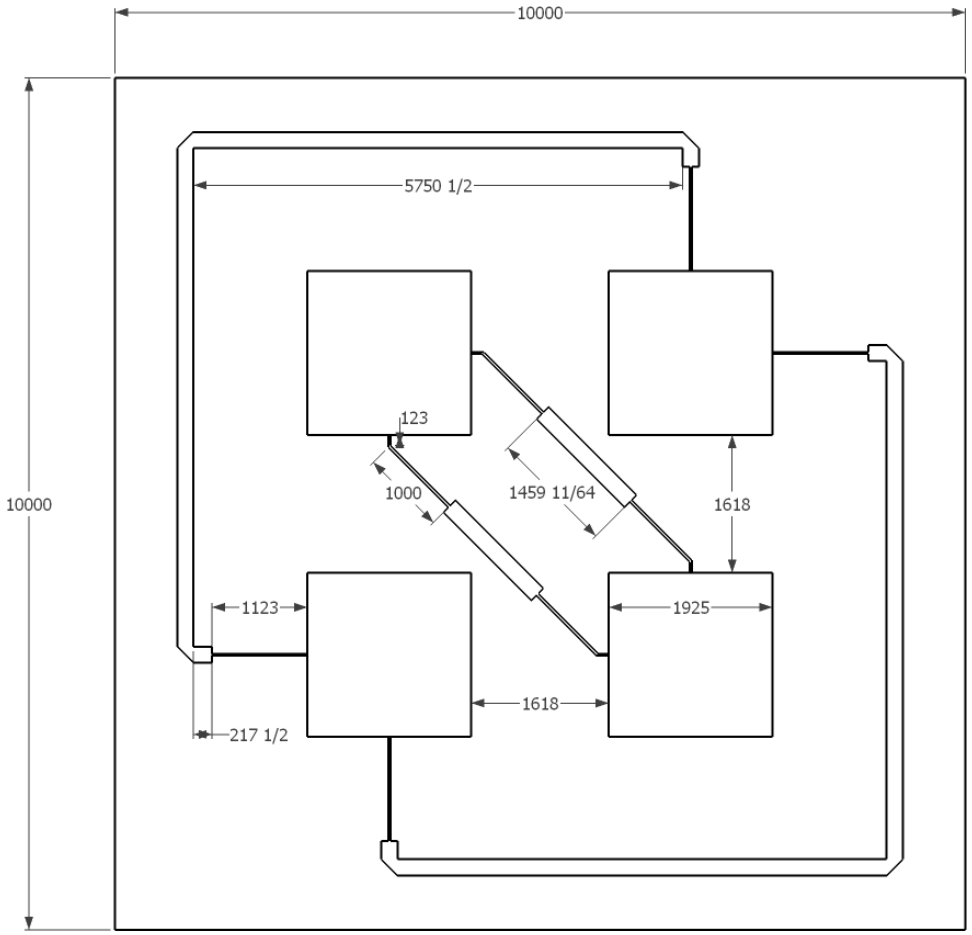

Figure 9. The design by Christodoulou and Chrissoulidis as modeled in SENTRi using PEC surfaces for patches, traces, and ground-plane with substrate height of 62 and lossless relative permittivity of ε_r=2.21 used, with all units in mils [3]**.**

Modifications for Microfabrication

Modification of the design by Christodoulou and Chrissoulidis is required to allow for microfabrication. The first step in the modification process is to remove the angled traces, which may not be accurately reproduced during microfabrication. All 45° angles are replaced with 90° angles, which are more compatible with direct-write lithography. The lengths of the transmission lines are adjusted to maintain a $2.5\lambda_g$ difference between the internal and external transmission line lengths. The external traces

lines are 13,964.5 mils and the internal trace lines are 2,915 mils. In the case of the 2-GHz design, the guided wavelength from Equation (1), Chapter 2, is 4,311 mils. The patch sizes remain unchanged from the design by Christodoulou and Chrissoulidis. However, the substrate size is changed to a 10-inch square from the 10-inch by 11-inch rectangle substrate used by Christodoulou and Chrissoulidis. For broadband performance evaluation 2-GHz is set as the center frequency.

The trace corners are modified to reduce excess line capacitance by implementing 0.7 trace width notch corners [23], as shown in Figure 10. While the best choice would be to keep filet corner on the traces, to allow for microfabrication, the design is restricted to right-angle features. The 0.7 trace width notch corner is considered a fair-to-good trace corner design [11] and is simplest to implement in this design.

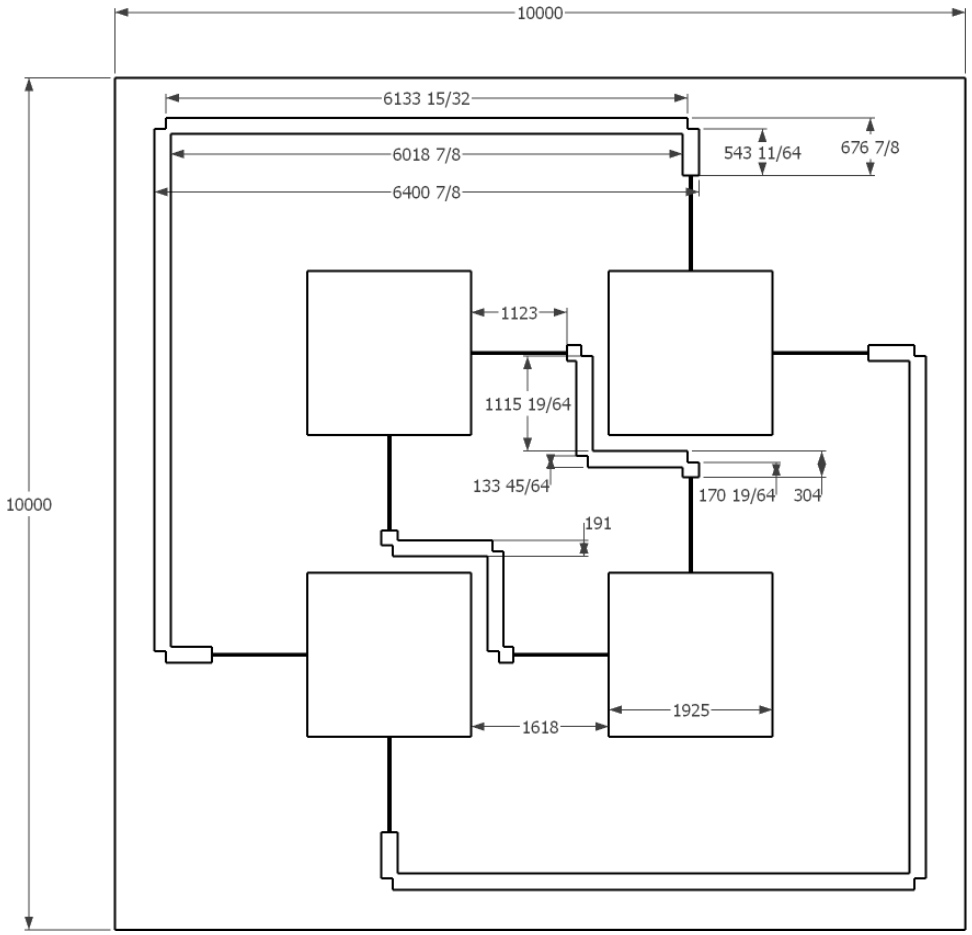

Figure 10. The design by Christodoulou and Chrissoulidis is modified with 0.7 width corner notches and meandering of interior traces, but maintaining PEC surface traces, patches, and ground plane with a substrate height of 62 and lossless relative permittivity of ε_r=2.21 (all units in mils).

Further modification is done by removing the quarter-wavelength transformers, which are not possible in the frequency-scaled design, resulting in Figure 11. Improved broadband performance is expected at the expense of center frequency peak performance.

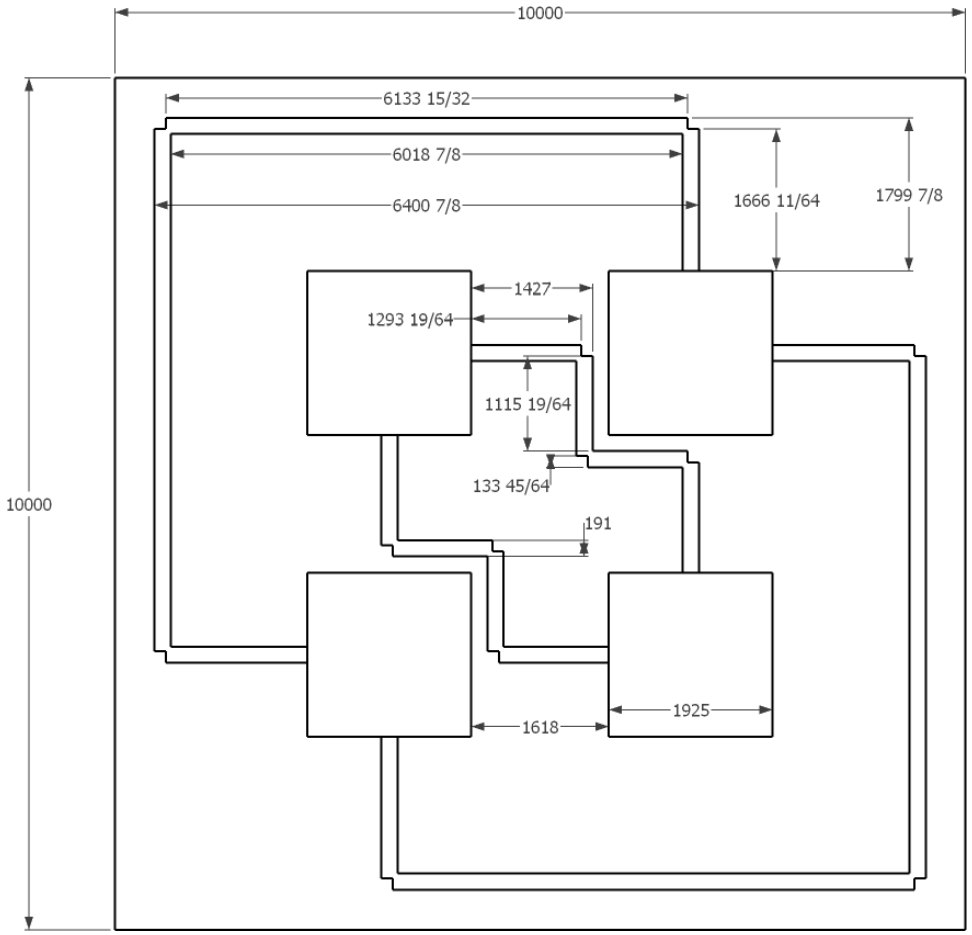

Figure 11. The design by Christodoulou and Chrissoulidis is modified sans transformers, but the PEC surface traces, patches, and ground plane are maintained. The substrate is unchanged with height of 62 and lossless relative permittivity of ε_r=2.21 (all units in mils).

These two modification steps are a prelude to the frequency scaling that will be done to accommodate the THz designs. The removal of the 45º corners and the quarter-wave transformers allows the design to be frequency scaled into nm sizes and meet microfabrication limitations. The transformers could not realistically be created on the nm scale. The expectation with the removal of the quarter-wave transformers is that broadband performance will improve, since the design is not as frequency-specific without the transformers. The focus of the analysis of these results is to isolate design

constrained performance changes from any frequency scaling induced performance changes.

THz Substrate Design Choice

Along with the modification of the original design to allow for microfabrication and broadband performance, an IR wavelength compatible substrate material must be chosen. Germanium is commonly used in IR applications, and has a high relative permittivity, which will reduce the thickness of substrate and theoretically improve broadband performance. However, patch and trace sizes may approach or fall below reasonable parameters. HfO_2 is frequency dispersive and has higher losses than Germanium in the long-wave-IR wavelengths. This could negatively affect broadband performance, but the relative permittivity is closer to unity at the center frequency, which will increase the patch and trace sizes to improve the coverage over the substrate.

The interest lies in the long-wave-IR, which is the bandwidth from 8 to 12 μm leading to the frequency range of 25 THz to 37 THz as derived in Equation (7).

$$
\begin{aligned}
f &= c/\lambda \\
f_{low} &= \frac{299792458\frac{m}{s}}{12\times10^{-6}m} = 25THz \\
f_{high} &= \frac{299792458\frac{m}{s}}{8\times10^{-6}m} = 37THz \\
\delta f &= f_{high} - f_{low} = 12THz \\
f_{center} &= \frac{299792458\frac{m}{s}}{10\times10^{-6}m} \approx 30THz
\end{aligned}
\tag{7}
$$

The square patch antenna is set as $\lambda_g / 2$, where λ_g is the guided wavelength, and $\lambda_g = \frac{\lambda_0}{\sqrt{\varepsilon_r}}$,where λ_0 is the wavelength in free space and ε_r is the relative permittivity of the separating material [24].

The relative permittivity for sputtered Ge is $\epsilon_r = 13.07$ at $10\,\mu\text{m}$ [25] leading to an effective wavelength in the substrate given by Equation (8) and patch size given by Equation (9).

$$\lambda_g = \frac{10\times10^{-6}\,\text{m}}{\sqrt{13.07}} = 2.8\times10^{-6}\,\text{m} \tag{8}$$

$$W = \frac{\lambda_g}{2} = 1.4\times10^{-6}\,\text{m} = 1.4\,\mu\text{m} = 1,400\,\text{nm} \tag{9}$$

Hafnium oxide has a relative permittivity of $\epsilon_r = 2.42$ at $10\,\mu\text{m}$ [25] leading to an effective wavelength in the substrate given by Equation (10) and patch size given by Equation (11).

$$\lambda_g = \frac{10\times10^{-6}\,\text{m}}{\sqrt{2.42}} = 6.4\times10^{-6}\,\text{m} \tag{10}$$

$$W = \frac{\lambda_g}{2} = 3.2\times10^{-6}\,\text{m} = 3.2\,\mu\text{m} = 3,200\,\text{nm} \tag{11}$$

As the patch is moved closer to the ground plane, less energy is radiated, and more energy is stored in the electric fields due to the capacitance and inductance of the patch. A rough equation for free space bandwidth from Dobkin, equation (6.21) [18] is shown in Equation (2) , Chapter 2. The impedance of free space is approximately $377\,\Omega$. The radiation resistance of a square patch antenna is typically around $150\ \Omega$ [18] leading

to Equation (3), Chapter 2. Solving for a 40% bandwidth, and using Equations (2) and (3), leads to Equations (12) and (13), that determine the dielectric thickness to be 470 nm for germanium and 1100 nm for hafnium oxide.

$$d = \frac{12\,THz}{30\,THz}\frac{1.4\times10^{-6}\,m}{1.2}$$
$$d = 4.7\times10^{-7}\,m = 470\,nm \tag{12}$$

$$d = \frac{12\,THz}{30\,THz}\frac{3.2\times10^{-6}\,m}{1.2}$$
$$d = 1.1\times10^{-6}\,m = 1{,}100\,nm \tag{13}$$

With the height of the dielectrics and the width of the patches determined, it is necessary to determine the size of the micro-strip lines that will be used to connect the patches. Using Balanis [17] equations (8-204 and 8-204b) for $W_{eff} < h$ and setting $Z_0 = 50\Omega$ allows us to find the effective width required for the transmission lines in Equations (14). For germanium, $W_{eff} = 321\text{nm}$ and $\varepsilon_{eff} = 8.57$. For hafnium oxide, $W_{eff} = 2{,}761\text{nm}$ and $\varepsilon_{eff} = 1.85$.

$$\varepsilon_{eff} = \frac{\varepsilon_r + 1}{2} + \frac{\varepsilon_r - 1}{2}\left[\left(1+12\left(\frac{h}{W_{eff}}\right)\right)^{-1/2} + 0.04\left(1-\left(\frac{W_{eff}}{h}\right)\right)^{2}\right]$$
$$Z_0 = \frac{60}{\sqrt{\varepsilon_{eff}}}\ln\left(8\frac{h}{W_{eff}} + 0.25\frac{W_{eff}}{h}\right)\Omega \tag{14}$$

To find the actual width required from the effective width, a thickness is required to be set. The minimum thickness depends on the skin depth of the metal to be used. The skin effect depth can be found from Equation (15) [8],

$$\delta = \sqrt{\frac{\rho}{\pi f \mu}} \ , \tag{15}$$

where δ is the skin depth, f is the desired operating frequency, ρ is the resistivity of the metal, and μ is the permeability of the metal. The approximate values of skin depth at $10\mu\text{m}$ are $\delta = 13.8nm$ for gold and $\delta = 15nm$ for aluminum. Good conductivity is achieved with a layer thickness that is 4-5 times the skin effect depth [18]. Choosing a thickness of $100nm$ allows for good conductivity, passivation oxidation, and consistent film uniformity [5, 8, 20]. Setting thickness to $t = 100nm$ leads to using Balanis [18] equation (8-206a) for $W > \frac{h}{2\pi}$ in Equation (16), which gives an actual width of $194\,\text{nm}$ for germanium and 2,600 nm for hafnium oxide.

$$W_{eff} = W + \left(\frac{1.25}{\pi}\right) \times t \times \left(1 + \ln\left(\frac{2h}{t}\right)\right) \tag{16}$$

The much smaller relative permittivity of hafnium oxide results in much larger patch sizes and transmission lines than the germanium design. Since the transmission line size at $Z_0 = 50\,\Omega$ is much too large to be practical for trace lines, a comparison was made of the size of the transmission lines from the previous designs. The transmission line width in the 2-GHz designs and the germanium substrate design is close to 10% of the width of the patch. The transmission line width for the hafnium oxide design should then be close to $320\,\text{nm}$ in order to meet the same ratio. Solving Equations (14)-(17) using a width of $320\,\text{nm}$ results in a $Z_0 = 125.45\,\Omega$. Rounding to the nearest integer and solving for $Z_0 = 125\,\Omega$ results in using a transmission line width of $330\,\text{nm}$. This width results in a change of effective permittivity such that $\varepsilon_{eff} = 1.87$ for hafnium oxide. The line loss of

the extra line impedance is expected to be offset by the better patch coverage offered by the lower effective permittivity at this scale.

It was determined from Equation (17) that the required size of the quarter-wave transformer required to impedance match the traces to the patches would have negative real width, which indicates model breakdown. A more complex model may lead to positive thickness, but the width would be very thin and difficult, if not impossible, to fabricate. This leads to the quarter-wave transformer being dropped for the refined design.

$$\begin{aligned} Z &= \sqrt{50 \times 377} = 137\Omega \\ W &= -119nm \end{aligned} \tag{17}$$

With the required dimensions determined, and keeping a $0.6\lambda_0$ distance between the centers of the patches to reduce mutual coupling, Table 1 lists the dimensions of the designs. The difference between trace lengths is $2.5\lambda_g$, the half wavelength offset is used to compensate for the change in the feeding side of the proposed design [3]. The germanium patches offer a 6.5% surface coverage of the substrate. While the larger patch sizes of the hafnium oxide do require a larger substrate, the result is still an improved coverage area with the hafnium design patches covering 12.6% of the substrate. This almost double coverage is expected to increase broadband retrodirective performance enough to offset the higher line impedance and frequency dispersive nature of the hafnium oxide at these wavelengths.

Table 1. THz design dimensions summary

	Germanium	Hafnium Oxide
Guided wavelength at 30 THz	2,800 nm	6,400 nm
Patch sizes	1,400 nm	3,200 nm
Trace width	194 nm	330 nm
Exterior trace lengths	17,520 nm	24,870 nm
Interior trace lengths	10,600 nm	8,800 nm
Trace length difference	6,920 nm	16,070 nm
Substrate width	11,000 nm	18,000 nm
Substrate thickness	460 nm	1,100 nm

Design Improvement and Substitution of Volume Elements for PEC Traces

Once a substrate choice between germanium and hafnium oxide has been determined, the design can be further refined. A relatively simple refinement is to reduce the transmission line lengths between the top right and bottom left patches to only $1.5\lambda_g$, which would reduce the trace lengths and the substrate size of a unit cell. The possibility of reduction to $1.5\lambda_g$ stems from the removal of the quarter-wave impedance transformers. The reduction in substrate size will result in in a higher percentage of surface area being covered by the patches.

The next step required is to replace the ideal conditions with measured material data by replacing the infinitely thin PEC patches and ground planes with volume elements using actual sputtered metal complex permittivities [25]. Gold and aluminum are both examined as possible materials. Gold has high conductivity, while aluminum has better direct adherence to the oxide substrate. The change in design will be to add a thickness to the ground plane and the patches not modelled when using the infinitely thin

PEC assumption as shown in Figure 12. Including a non-PEC ground plane will affect the field grounding into it and add losses due to the skin effect of the metal ground plane.

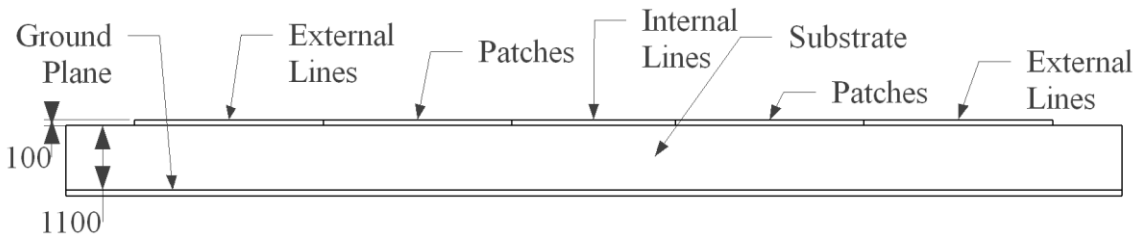

Figure 12. An illustrated example of sputtered metal layers separated by a dielectric substrate, assuming hafnium substrate is used the metal layers will be 100 nm thick over a 1100 nm substrate (units are in nm)

Summary

A method was defined for scaling the 2-GHz design described by Christodoulou and Chrissoulidis [3] to operate at 30 THz by making incremental changes. The modeling and simulation of each step of the process was proposed to examine how each change affects the performance. In this vein, the evaluation of the accuracy of simulation results by performing solution convergence tests on local machines with more RAM was also described. Modeling the frequency scaled design using both germanium and hafnium oxide as substrate materials provides two possible THz scaled design results for performance comparison. Based upon the performance of the frequency-scaled designs, further refinement of the chosen design using the substrate material that performs the best was proposed. In particular, implementing measured data as volume elements for sputtered metal in place of infinitely thin PEC patches and ground plane, is suggested. Chapter 4 discusses the results and analysis from the simulations run.

IV. Analysis and Results

Solution convergence analysis

Solution convergence is desired to indicate that solution from the model is viable. Using the published 2 GHz centered design, the global mesh sizing variable in Capstone is progressively decreased, while the minimum size variable is maintained at 25 mils and the size increment ratio variable is set to 1.2, to provide transitions between coarser and finer meshes. Eleven meshes were created, using the compound parametric mesher in Capstone [9] to create both volume and surface meshes, with the attributes shown in Table 2. Ten of the meshes were then simulated in SENTRi at excitation angles $\phi = 0°$ and $\theta = 20°$, where ϕ is angle of rotation in the xy-plane from the x-axis and θ is the angle from the z-axis. The 11th mesh required more memory than was available.

Table 2. Convergence mesh attributes

Mesh	Memory (GB)		Global Sizing	Vertices	Simulation Time
	Minimum	Recommended			
1	3	6	500	6114	00:16:45
2	4	8	250	7312	00:22:46
3	6	11	200	8782	00:36:45
4	12	19	150	12240	00:58:38
5	21	32	125	16458	01:49:48
6	27	41	115	18763	02:50:29
7	32	47	110	20357	03:19:35
8	43	63	100	24002	06:25:07
9	64	91	90	29259	08:35:36
10	100	138	80	36541	14:27:56
11	128	175	75	41448	N/A

For visual reference, Figure 13 shows examples of four different mesh densities. Values for the backscatter radar cross section (RCS) were then calculated as shown in Figure 14.

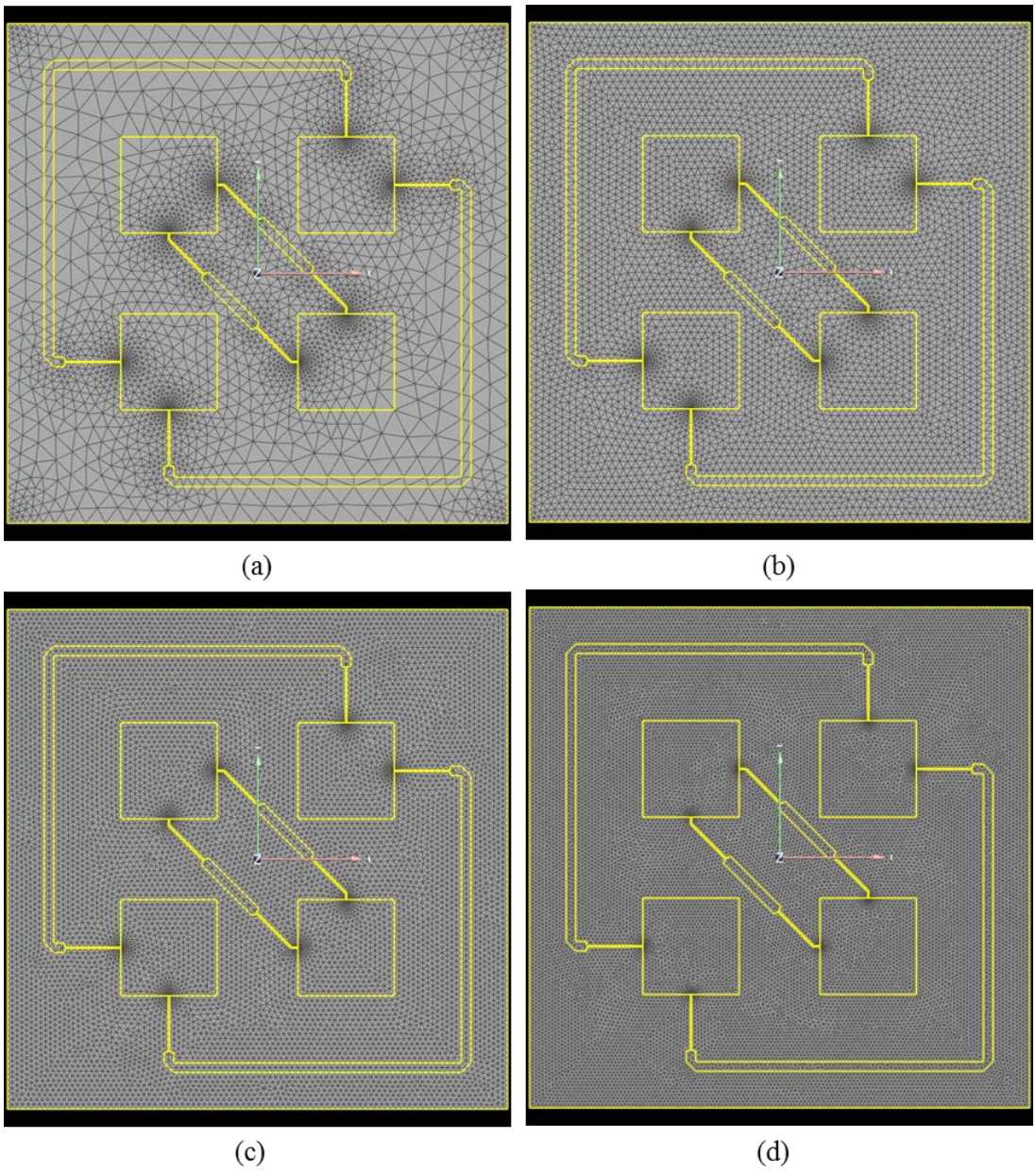

Figure 13. Sample of meshes used showing progressively finer meshes with global mesh sizing values of (a) 500, (b) 150, (c) 110, and (d) 90 mils.

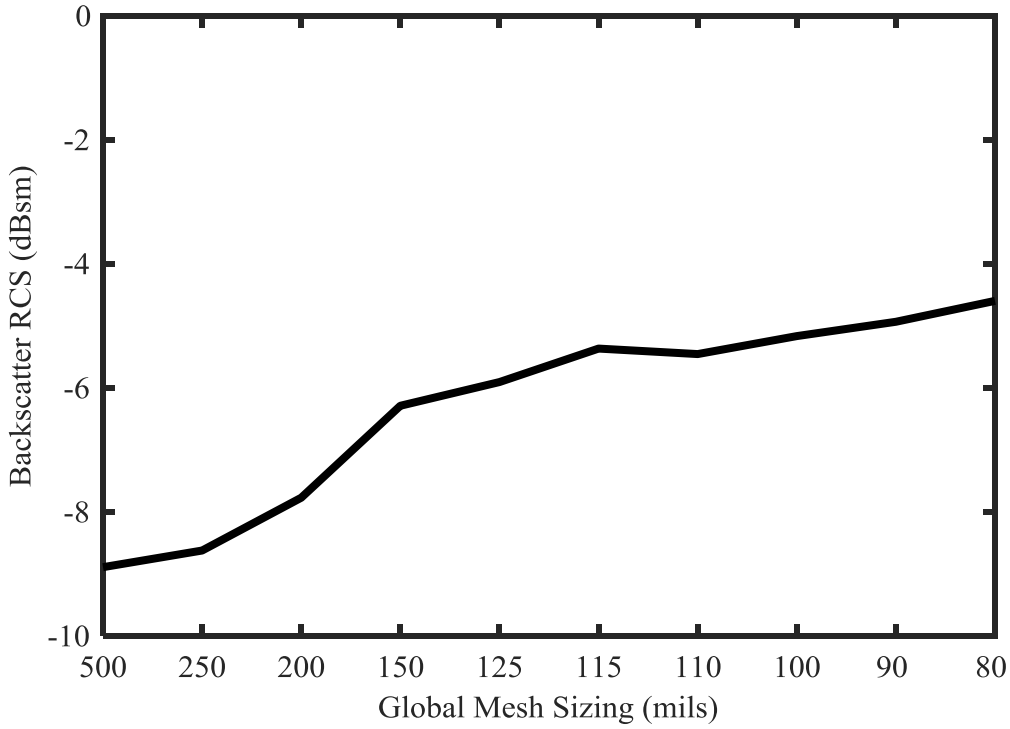

Figure 14. Backscatter RCS (dBsm) showing the backscatter RCS value as mesh density is increased and how the rate of change has a knee around the global sizing 115 mil, which was the maximum density possible with the limited RAM available on the HPC resources used.

Table 2 shows global size 115 is the highest density mesh the HPC resources used can support, with the limited memory per node available. From Figure 14 global size 115 can be seen as the point where the rate of change has slowed down. The difference from global size 115 to global size 90 is less than $1 dB$, which is a reasonable margin of error [26]. The HPC results are considered viable, though note that other HPC resources (i.e. Thunder server) with higher memory per node architecture, could be used to further refine results if available.

Analysis of the 2-GHz Design by Christodoulou and Chrissoulidis

The design by Christodoulou and Chrissoulidis was recreated in Capstone and simulated in SENTRi using the same values as published [3] as shown in Figure 9. Metal patches and transmission lines are represented as infinitely thin PEC surfaces. Substrate height of 62 mils and patch widths of 1,925 mils were used. The model was then simulated in SENTRi with bottom surface, patches and transmission lines all modeled as PEC, and all other exterior surfaces modeled as transparent. The interior volume was modeled as lossless with $\epsilon_r = 2.21$ [3].

Thirty-one different frequencies from 1.67 GHz to 2.5 GHz were modeled to evaluate 40% bandwidth broadband performance. The model was excited using ϕ values from $-180°$ to $180°$ with $\Delta\phi = 9°$, θ values from $0°$ to $60°$ with $\Delta\theta = 10°$, for each frequency. The θ values were limited to 60° to match the published results and to take into account that the intended application would not have near grazing angles. The 2-GHz results were then compared to Figures 4 and 6 in the published results [3]. Figure 15 shows that retrodirectivity is achieved and is similar to the results seen in Figure 4 of the published results [3], except that simulated results show the peak shifted to 10° instead of the expected 20°. Figure 16 shows the beamwidth of the retrodirective behavior and indicates a 3dB drop occuring at approximately 40° from center, which agrees with the published conclusion of 80° beamwidth.

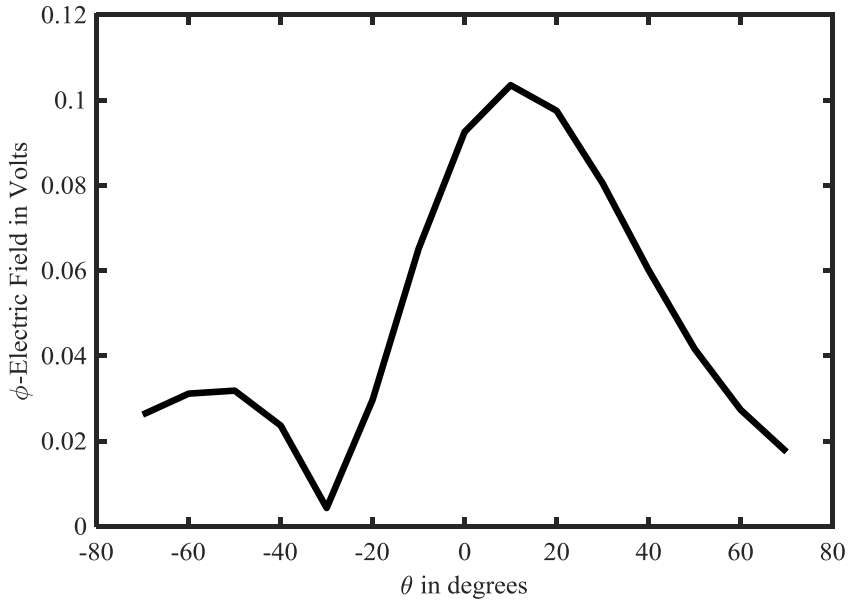

Figure 15. The bistatic retrodirective action of modeled design based on Christodoulou and Chrissoulidis [3] **shows a peak of retrodirectivity at 10° which is shifted slightly from the published result of peaking at 20°, but does confirm cross-pol retroreflective action.**

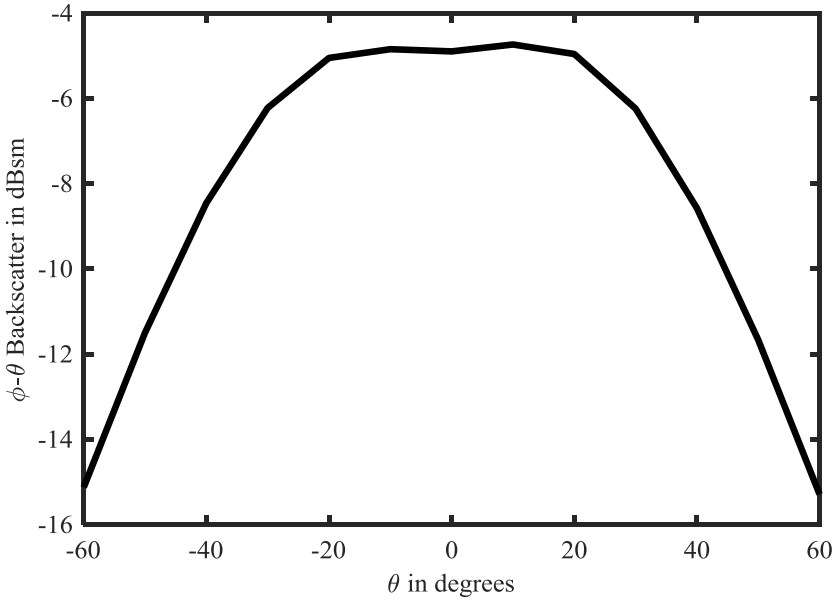

Figure 16. The monostatic backscatter RCS of modeled design based on Christodoulou and Chrissoulidis [3] **with phi fixed at 90° shows approximately 80° beamwidth before the -3 dB points at 40° and -40°, which agrees with the published results.**

Using the same model but with all exterior surfaces set to PEC, a flat plate was simulated. For comparison to other designs the simulated RCS (dBsm) values are normalized using MATLAB by subtracting the flat plate backscatter RCS values from the modeled design backscatter RCS in Equation (18). The normalized results are then converted to linear values in Equation (19). With the resulting array of 8,897 linear ratios, a bandwidth normalized ratio is found by summing all linear values and dividing by the number of angles of excitation, per Equation (20), to give a single linear ratio number. The area, frequency, and angle are normalized for comparison purposes across all designs. The resulting ratio is used to compare the performance of all 2-GHz modifications and 30-THz designs. The design by Christodoulou and Chrissoulidis gives a linear backscatter ratio of 119.26. This number was the baseline for comparison and any design that gave a higher linear ratio was considered to have better broadband performance than the design by Christodoulou and Chrissoulidis. Figure 17 shows an example of the normalization process, demonstrating the improvement in RCS over a flat plate that the design by Christodoulou and Chrissoulidis exhibits at 2 GHz. However, the final ratio number has all 31 different frequencies included in order to compare broadband performance, as shown in Table 3.

$$RCS_{norm} = RCS_{design} - RCS_{plate} \tag{18}$$

$$RCS_{linear} = 10^{\frac{RCS_{norm}}{10}} \tag{19}$$

$$Ratio_{linear} = \frac{\Sigma(RCS_{linear})}{\#of\ angles} \tag{20}$$

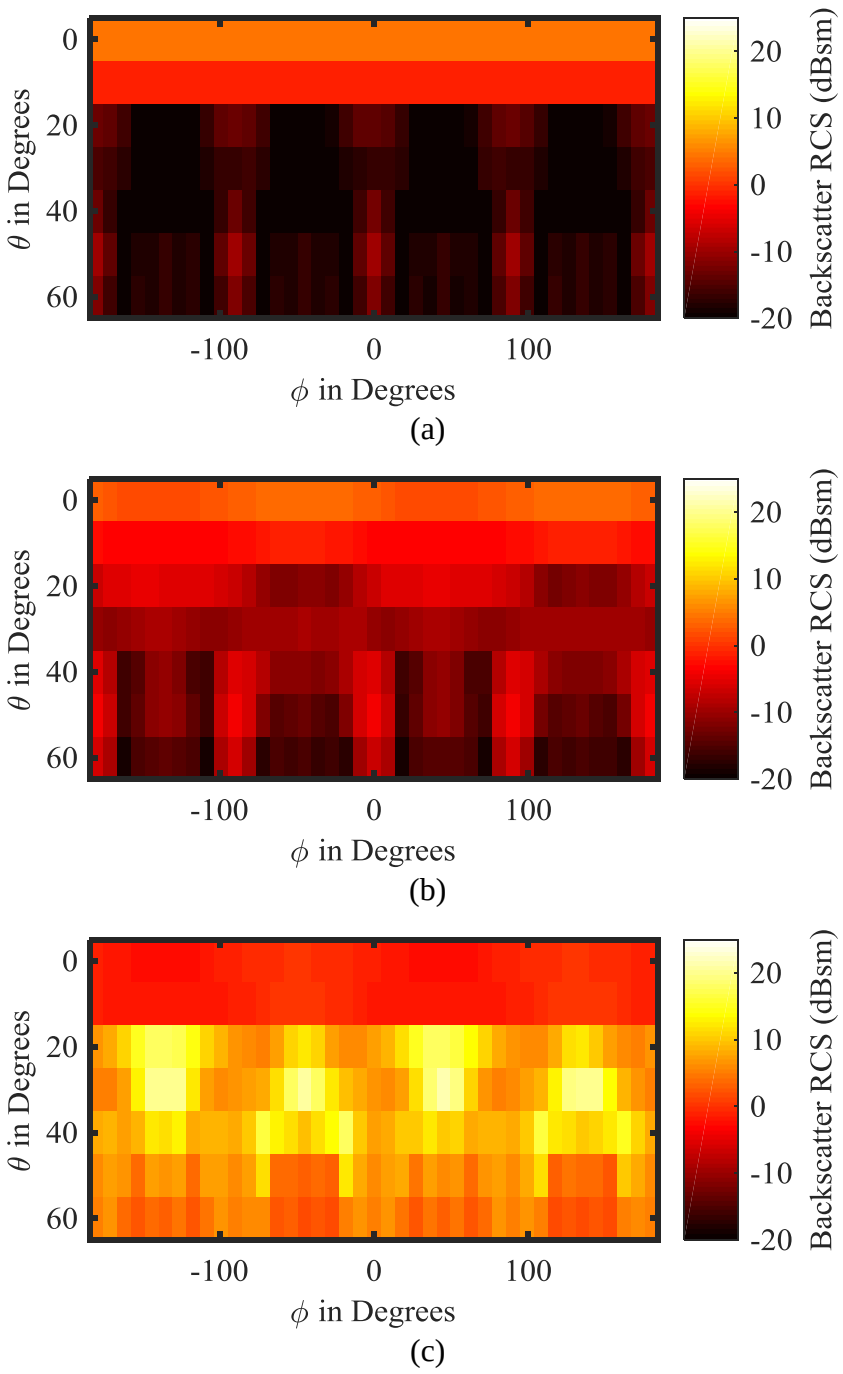

Figure 17. Visual representation of normalization process at 2 GHz (a) Flat Plate RCS (b) Design by Christodoulou and Chrissoulidis RCS (c) Design by Christodoulou and Chrissoulidis RCS – flat plate RCS, showing the improvement over the flat plate exhibited by the modeled design. The 0° and 10° θ regions of the plots show that almost no difference occurs between a flat plate and the design showing that near zenith angles have behavior similar to that of the flat plate.

2-GHz Design Modification Analysis

The modified design was created from the same basic dimensions as the design by Christodoulou and Chrissoulidis. The interior trace lines were replaced with meandering lines that created a length of 2,915 mils and external traces lines were set to 13,964.5 mils as shown in Figure 10. The resulting RCS values are normalized. The modified design gives a linear backscatter ratio of 124.18, which is a 4% broadband performance improvment over the design by Christodoulou and Chrissoulidis. The 2 GHz response is shown shown in Figure 18. The improvement may be attributed to a slight increase in surface area covered by the transmission lines, most importantly the result shows that meandering the interior transmission lines and using the 70% trace corner notch does not have a substational negative impact on the performance of the design, in broadband role operation.

The design is further modified by removing the transformers from the modified design as shown previously in Figure 11. The modified design without transformers gives a linear backscatter ratio of 127.88, which is a 7% broadband performance improvement over the design by Christodoulou and Chrissoulidis and a 3% broadband performance improvment over the modified design, the 2 GHz as shown in Figure 19. The improvement of this design modification was expected as the design is not as frequency specific without the transformers and therefore has a better broadband response.

The modified designs showed peak performance off of the designed peak of 2 GHz. Appendix A further explores the details of the change of center frequency, comparing frequency response across all designs.

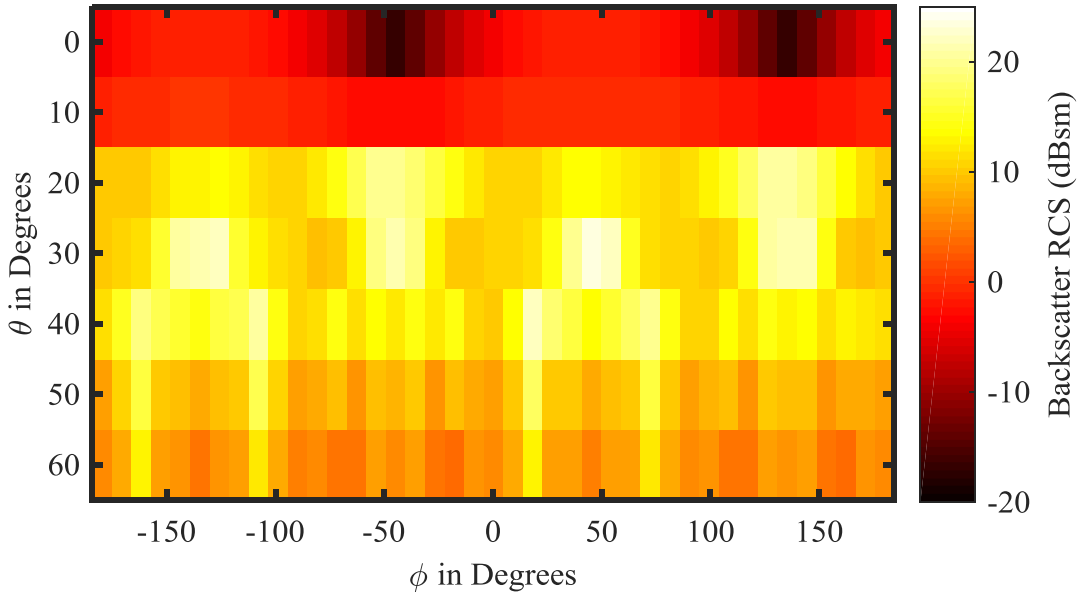

Figure 18. Modified design normalized backscatter RCS performance at 2 GHz showing similar performance to the published design, which reinforces the idea that these modifications does not have a substantial negative impact on the performance of the design.

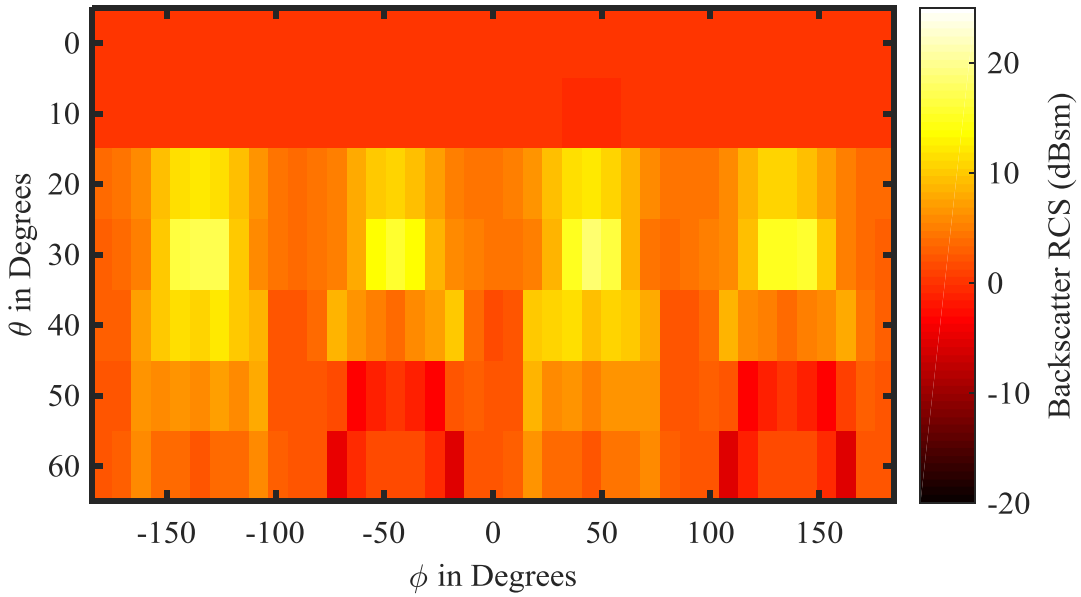

Figure 19. Transformerless design normalized backscatter RCS performance at 2 GHz shows a decrease in performance at 2GHz indicating that removing the transformers may have affected the center frequency of operation. An analysis in Appendix A supports this indication.

Table 3. 2-GHz design performance factor comparison

Design	Linear RCS Ratio	Performance Factor
Published design	119.26	1.00
Initial modification	124.18	1.04
Modification sans transformers	127.88	1.07

30-THz Germanium Design Analysis

Using sputtered germanium as the substrate dielectric, the patches are 1,400 nm square and 100 nm thick, the substrate is 11,000 nm square and 460 nm thick, with 10,600 nm long interior traces, and 17,520 nm long exterior traces. The reference flat plate is created by changing all exterior surfaces of the germanium design to PEC in SENTRi. The normalization is then accomplished by subtracting the flat plate RCS from the germanium substrate RCS. The resulting linear backscatter ratio is 47.50. The result shows an approximate decrease in performance of 60%, which is explained by the much smaller portion of the surface area covered by the patches, as shown in Figure 22. The large relative permittivity, shown in Figure 20 over the 8-12 μm regime, provided by the germanium may improve bandwidth and decrease the required substrate height, but it causes the patches to be too small to be effective in this design. From the analysis in Appendix A, the design peaks at 36.6667 THz, which is well off from the design frequency at 30 THz. Figure 21 shows normalized backscatter RCS performance at 30 THz. This result can be compared to the results shown in Figures 17-19. Further modification of the design might allow better centering of the performance and overall improvement of broadband performance. However, the level of performance observed does not merit further refinement in this research.

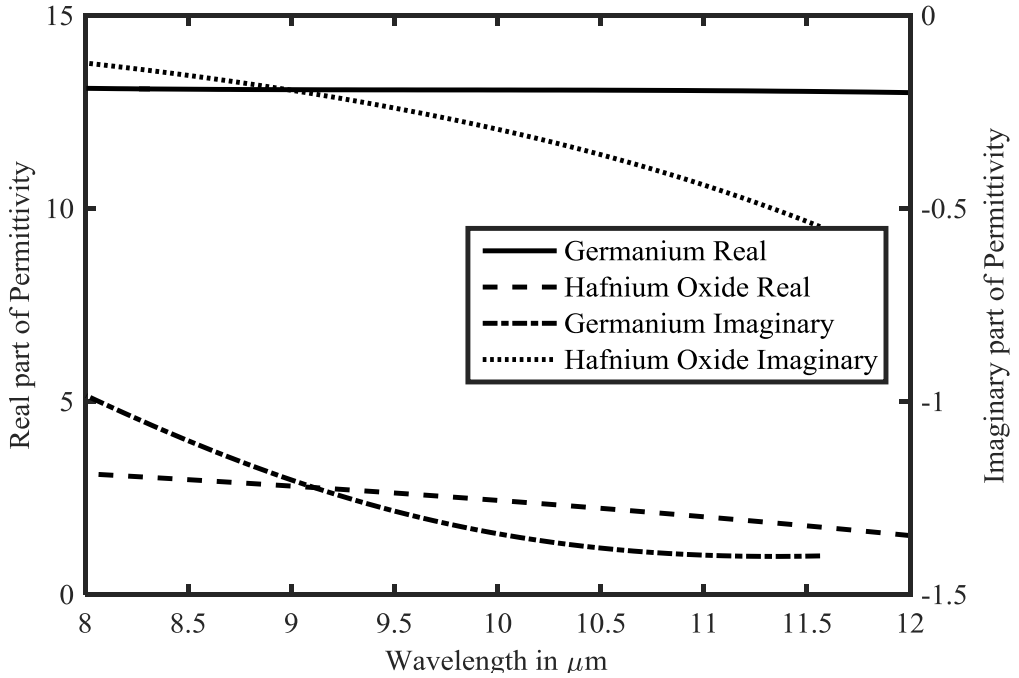

Figure 20. The sputtered substrate material complex permittivity shows the difference in permittivity values between germanium and hafnium oxide, where germanium shows higher real permittivity, and the loss component is much higher in the hafnium oxide [25].

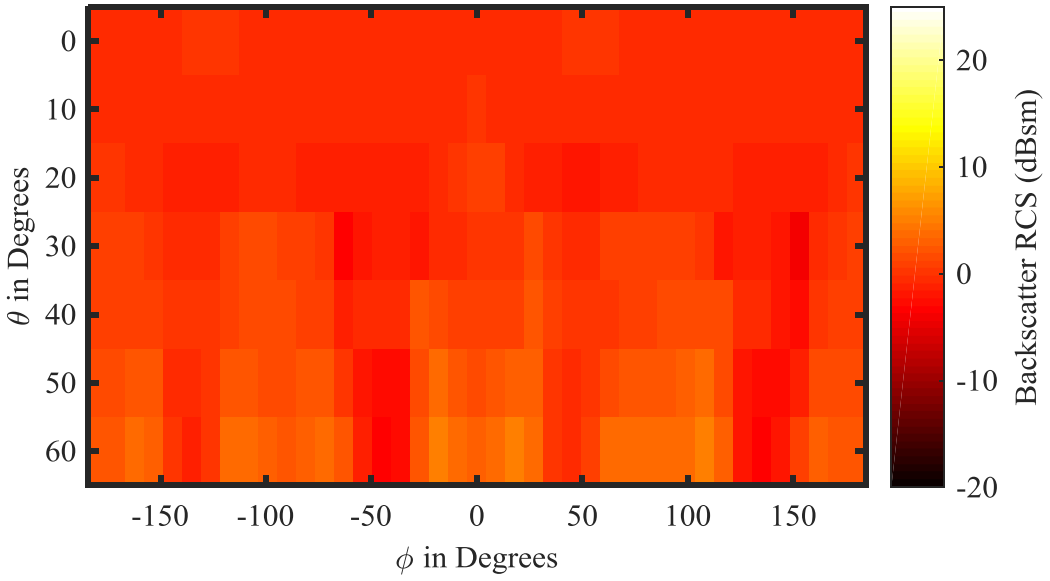

Figure 21. The germanium substrate normalized backscatter RCS at 30 THz showing relative performance lower than that of the GHz designs.

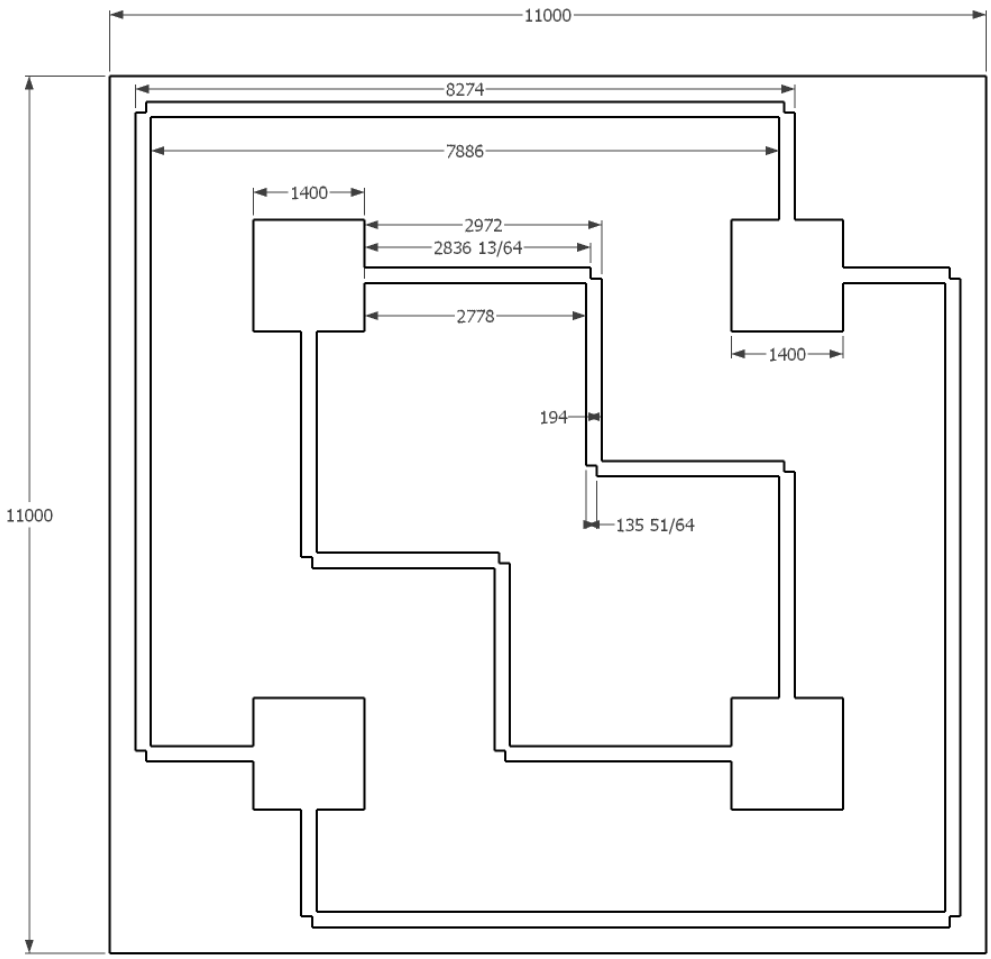

Figure 22. The germanium substrate design with PEC surface traces, patches, and ground plane, with the substrate with height of 400 and frequency dispersive complex permittivity from Figure 20 (all units in nm).

30-THz Hafnium Oxide Design Analysis

Using hafnium oxide as the substrate material, the patches are 3,210 nm square and 100 nm thick, the substrate is 18,000 nm square and 1,100 nm thick, with 8,790 nm long interior traces, and 24,860 nm long exterior traces. The reference flat plate is created by changing all exterior surfaces of the hafnium oxide design to PEC in SENTRi. The normalization is then accomplished by subtracting the flat plate RCS from the hafnium

oxide substrate RCS. The resulting linear backscatter ratio is 514.25, which is a 330% broadband performance improvent over the design by Christodoulou and Chrissoulidis. This result shows a large increase in performance due to the low relative permittivity of hafnium oxide that creates a larger patch area coverage over the substrate than any previous design, as shown in Figure 23. The low relative permittivity, indicated in Figure 10, has a negative effect on the broadband performance, but the closer impedance matching between the traces and patches, caused by the higher effective wavelength and increase in patch coverage appear to offset the performance losses of the low dielectric and higher line impedance. Given that the lengths of the traces are at most four guided wavelengths; the higher impedance traces appear to have been a good trade. Figure 24 shows normalized backscatter RCS performance at 30 THz. This result can be compared to the results shown in Figures 17-19. Table 4 shows the resulting performance factors of the germanium and hafnium oxide substrates. This sets hafnium oxide as the substrate of choice, over germanium, to further refine and model with metal volume elements.

Table 4. 30 THz design performance factor comparison between germanium and hafnium oxide substrates

Design	Linear RCS Ratio	Performance Factor
Published design	119.26	1.00
Germanium substrate	47.50	0.40
Hafnium oxide substrate	514.25	4.31

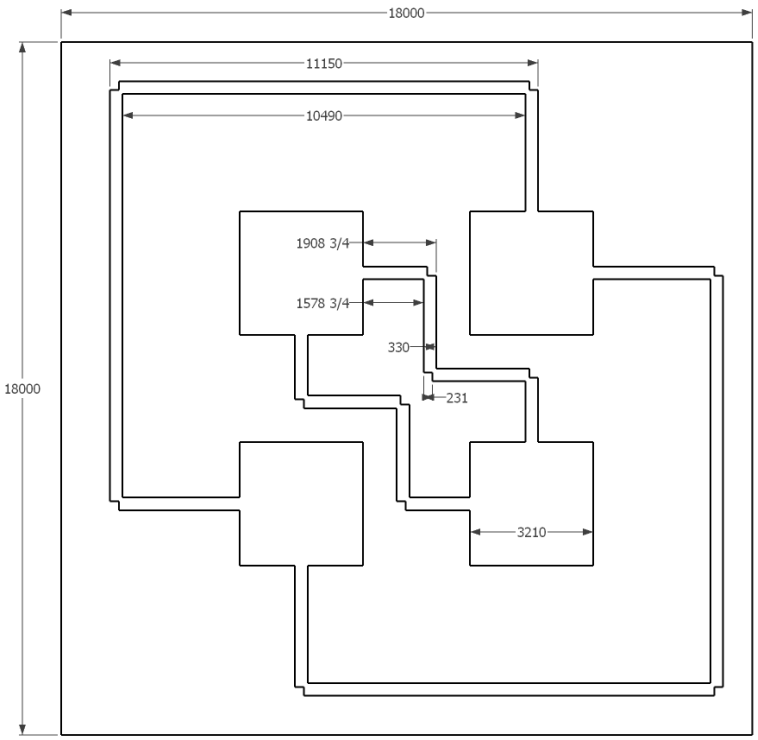

Figure 23. The hafnium oxide substrate design with PEC surface traces, patches, and ground plane, with the substrate with height of 1,100 and complex permittivity from Figure 20 (all units in nm).

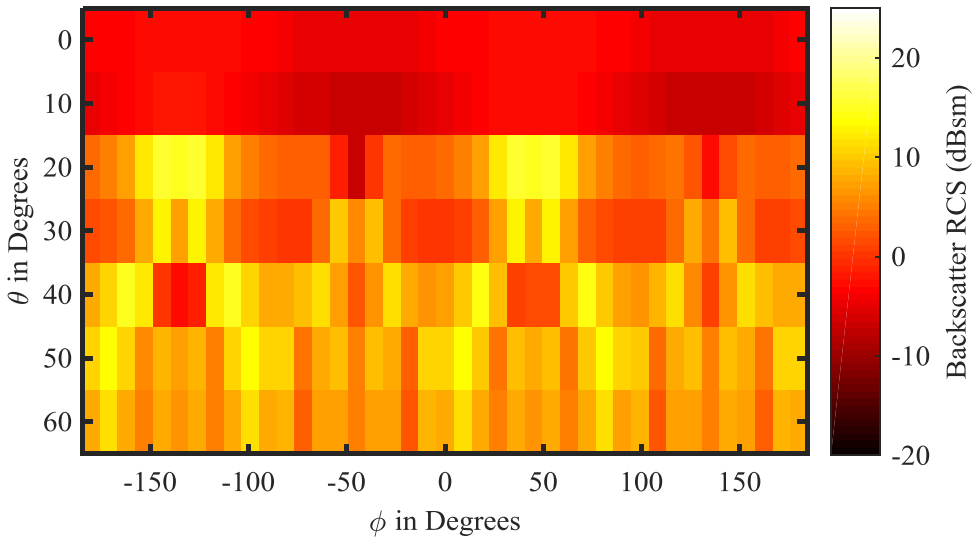

Figure 24. The hafnium oxide substrate normalized backscatter RCS at 30 THz showing relative performance higher than that of the GHz designs.

30-THz Hafnium Oxide Design Refinement

As a refinement to the hafnium oxide design, the exterior traces are reduced in length from a $2.5\lambda_g$ to a $1.5\lambda_g$ difference from the interior trace lines. The $0.5\lambda_g$ difference is maintained for the orthogonal feed compensation, but the shortening of the trace lengths will reduce losses in the transmission line and allow a reduction in substrate size, which will cause an increase in the patch coverage ratio. The resulting linear backscatter ratio is 246.05. This result is surprising since both changes that came from shortening the outside traces were expected to have improved performance. Examining the design, as shown in Figure 25, the hypothesis is that since the trace line stubs coming out of the patches are now approximately $\lambda_g / 4$ long to the notched corner, there could be some destructive interference, whereas the previous design had $\lambda_g / 2$ long stubs. Comparing Figure 26 and Figure 27 shows the difference in the surface field phase plots from SENTRi for the $1.5\lambda_g$ design and the $2.5\lambda_g$ design, respectively. The results suggest that destructive interference occurs due to the quarter wavelength difference between the two different impedance points of the patch and the notch corner on the exterior traces, while the interior traces remain unchanged.

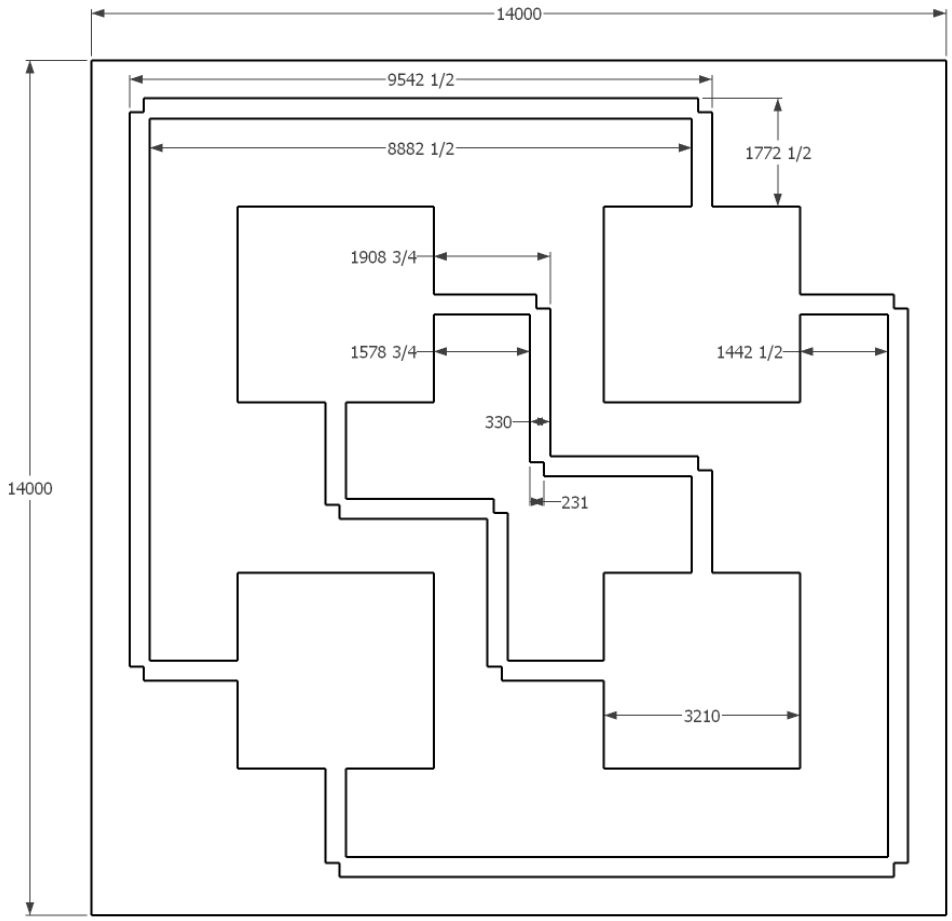

Figure 25. The further modification of the hafnium oxide substrate design with shorter external traces and smaller substrate, but maintains PEC surface traces, patches, and ground plane, with the substrate with height of 1,100 and complex permittivity from Figure 20 (all units in nm).

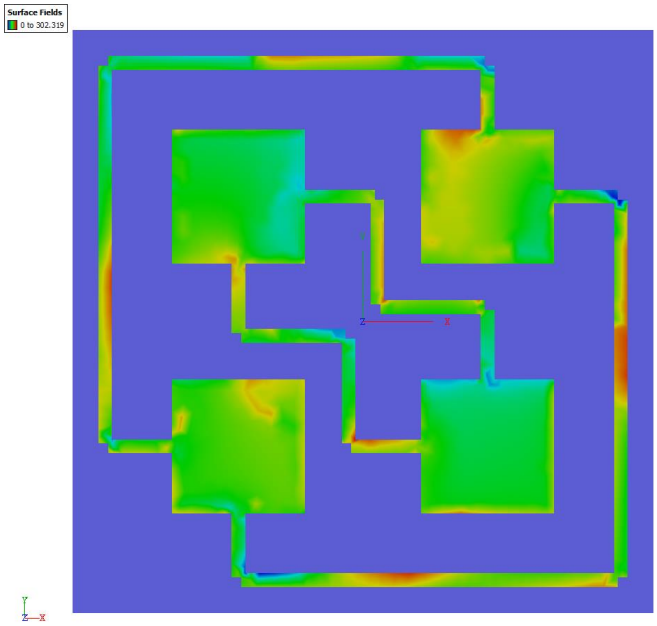

Figure 26. The surface fields at 30 THz and $\theta = 20°$ and $\phi = 0°$ excitation of hafnium substrate with 1.5λ trace length difference showing phase of electric field.

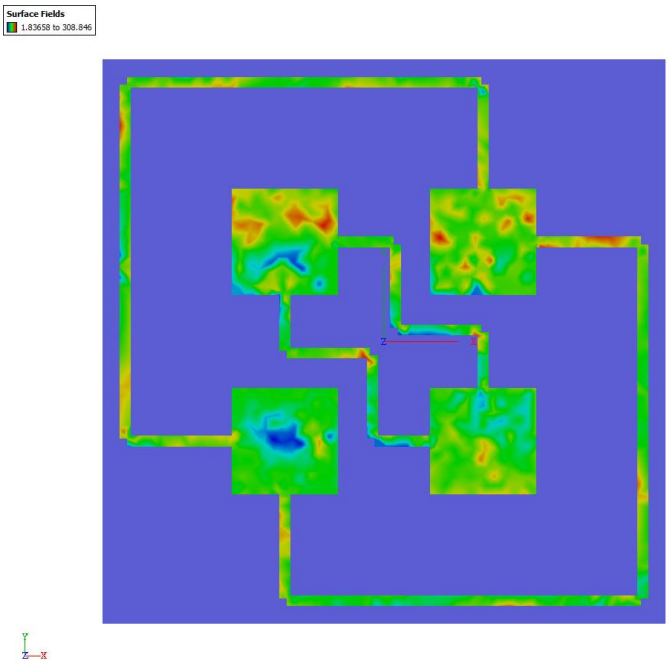

Figure 27. The surface fields at 30 THz $\theta = 20°$ and $\phi = 0°$ excitation of hafnium substrate with 2.5λ trace length difference showing phase of electric field.

Although the results did not show that the $1.5\lambda_g$ design change improved the performance as expected, the possibility that replacing the PEC surfaces with sputtered metal volume elements may overcome the performance losses will be investigated. The metal designs will be modeled with both lengths of traces to examine the effects of using volume elements in place of PEC surfaces.

30-THz Hafnium Substrate Metal Trace Designs Analysis

Using both of the hafnium oxide designs, the patches, line traces, and ground plate are replaced with $100nm$ thick gold or aluminum volume elements, using permittivity data that was measured on sputtered films by the Air Force Research Laboratory Materials and Manufacturing Directorate, the values of which are shown in Figure 28. The linear ratios, shown in Table 5, met the expectations of refining the hafnium oxide design. The volume element simulation included enough other variables to overcome the $\lambda_g / 4$ long stubs that the outside trace lines have, with 30 THz RCS backscatter shown in Figure 31. The added oxide bonding and cost advantages of aluminum over gold lead to a probable overall advantage for aluminum. Figures 30 and 31 show normalized backscatter RCS performance of the gold and aluminum designs respectively at 30 THz. This result can be compared to the results shown in Figures 17-19.

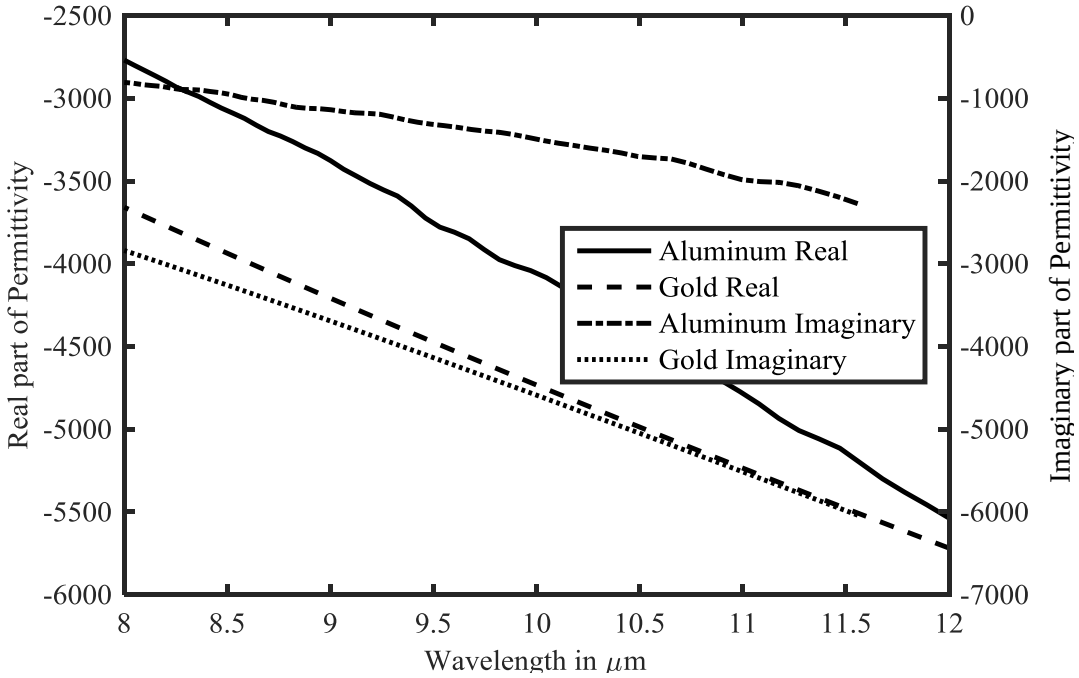

Figure 28. Permittivity data of sputtered metals showing both real and imaginary components.

Table 5. Linear RCS ratios of metal designs showing broadband performance improvement over design by Christodoulou and Chrissoulidis.

Design	Linear RCS Ratio	Performance Factor
Published design	119.26	1.00
Gold (2.5λ)	391.07	3.28
Gold (1.5λ)	432.00	3.62
Aluminum (2.5λ)	385.63	3.23
Aluminum (1.5λ)	423.16	3.55

To close the design loop, the solution convergence of the aluminum design was verified for the volume meshed elements. The results in Figure 29 and tabulated in Table 6 show a reasonable expectation that the simulation is under predicting the retro results, rather than over predicting. The results were obtained using $\theta = 20^{\circ}$ and $\phi = 0^{\circ}$ to 180° with $\Delta\phi = 22.5^{\circ}$ and averaging the RCS values.

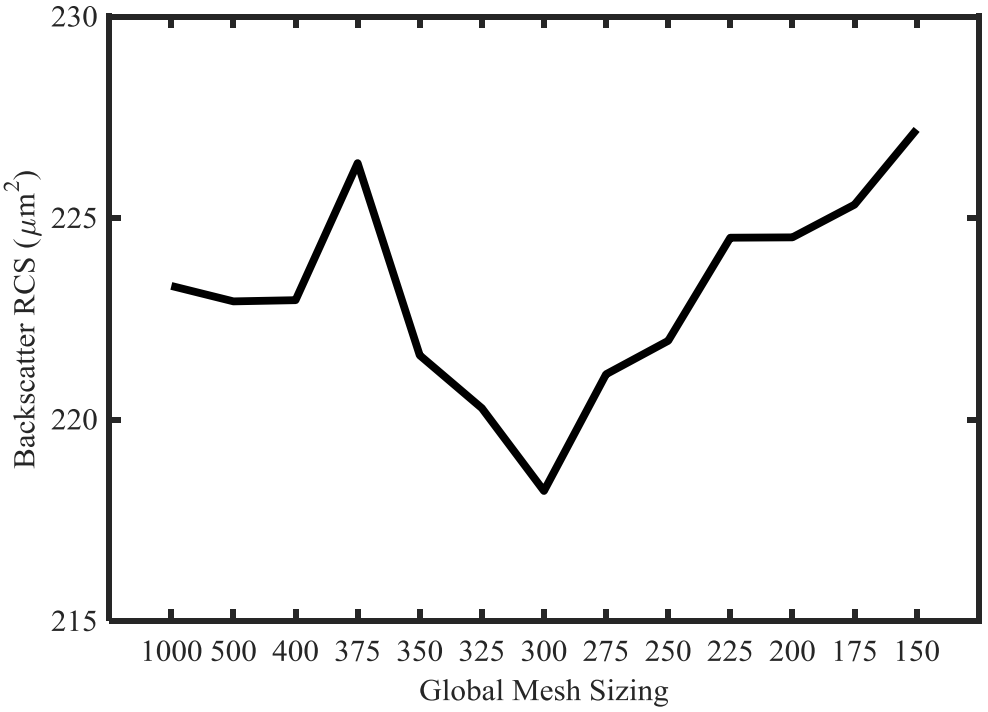

Figure 29. Aluminum design backscatter RCS (μm^2) values at decreasing mesh densities.

Table 6. Aluminum mesh convergence

Global Sizing	Memory (GB)		Backscatter RCS (μm^2)
	Minimum	Recommended	
1000	13	35	223.3146
500	13	35	222.9316
400	14	38	222.9614
375	15	39	226.3627
350	16	42	221.5932
325	18	46	220.2810
300	20	51	218.2268
275	24	105	221.1231
250	29	72	221.9532
225	19	45	224.5114
200	26	60	224.5202
175	39	87	225.3309
150	66	139	227.1980
125	131	256	N/A

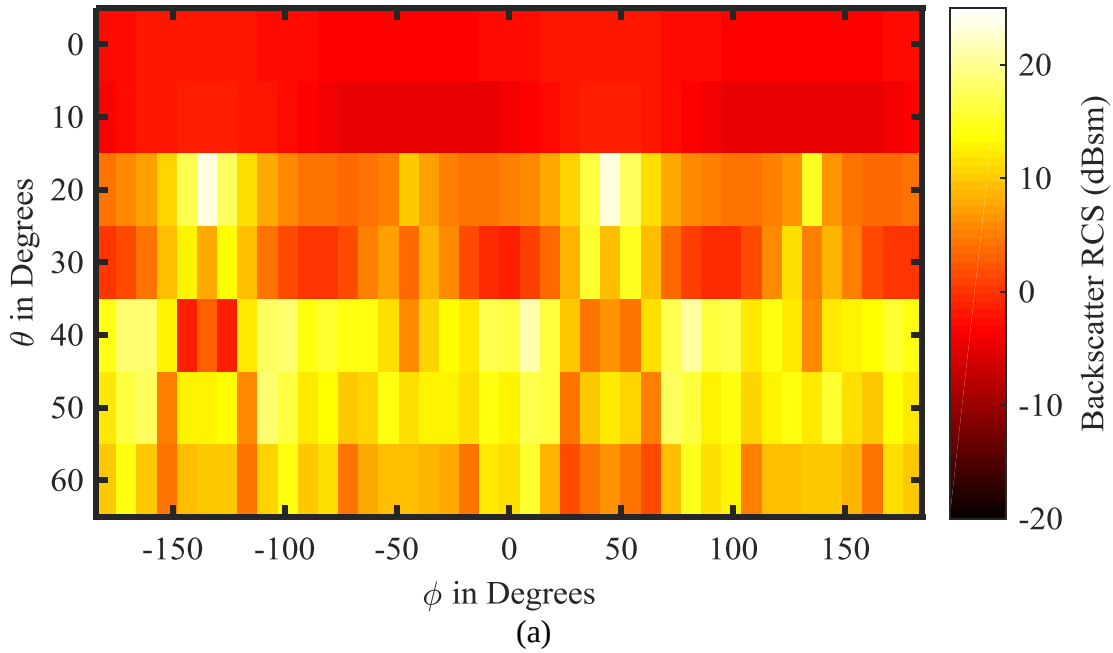

(a)

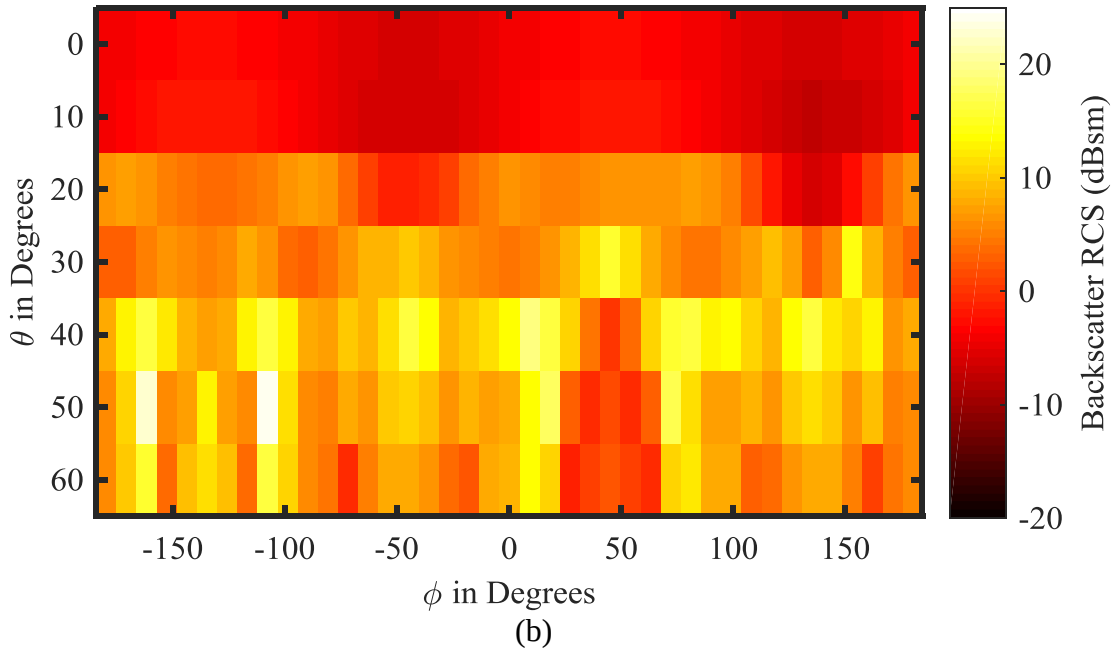

(b)

Figure 30. Gold design normalized backscatter RCS (dBsm) at 30 THz (a) $2.5\lambda_g$ (b) $1.5\lambda_g$ shows that the center frequency of performance may shift when shortening the external trace lengths, but there is better performance at higher θ angles which may be desirable in some applications.

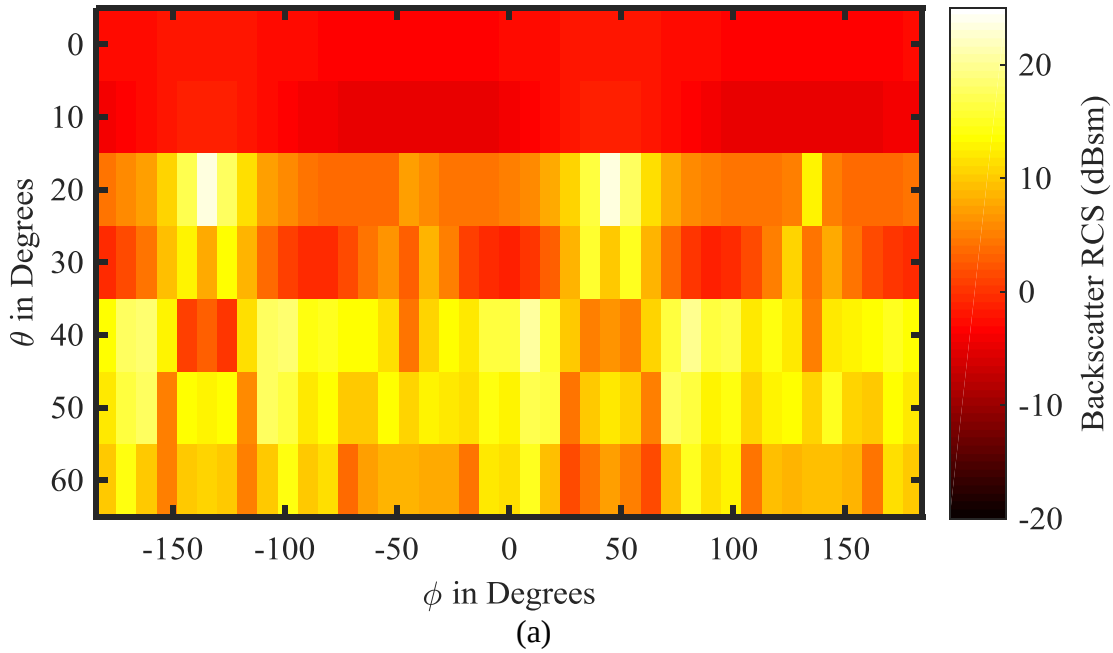

(a)

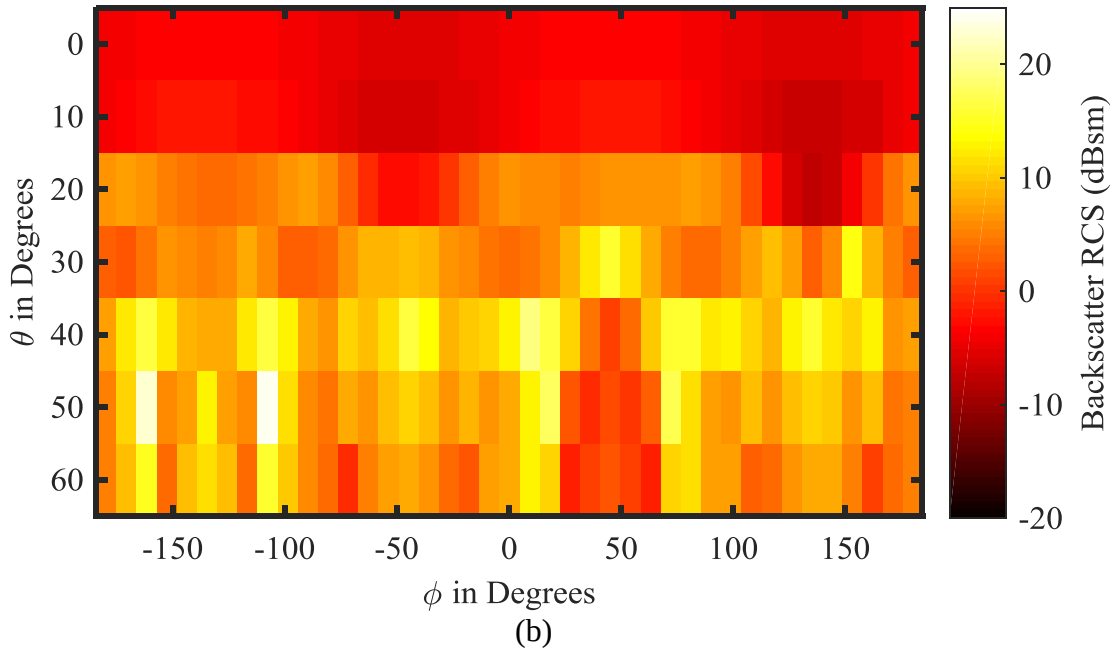

(b)

Figure 31. Aluminum design normalized backscatter RCS (dBsm) at 30 THz (a) 2.5λ_g (b) 1.5λ_g shows very similar performance to the gold design in both cases again showing better performance at higher θ angles with the shorter external trace lengths.

Further analysis of the aluminum design was done to explore the final design in more detail. Figure 32 shows the same monostatic measurement that was done on the baseline design to compare it to Figure 4 of the published results [3]. The peak at 5° is off from the desired 20° peak, but still shows retrodirective behavior. A peak at -20° would have shown specular behavior from the 20° excitation. Figure 33 shows the same bistatic measurement that was done on the baseline design to compare to Figure 6 of the published results [3]. The figure shows that the 3dB retrodirective beamwidth has dropped from approximately 80° to approximately 35°, ranging from -15° to 20°. Running another SENTRi simulation with more angles of interest to get a finer backscatter RCS plot resulted in the normalized backscatter plot at 30 THz shown in Figure 34. Thirty-one different frequencies from 25 THz to 37.5 THz were modeled to evaluate 40% bandwidth broadband performance. The model was excited using ϕ values from $-180°$ to $180°$ with $\Delta\phi = 12°$, θ values from $0°$ to $60°$ with $\Delta\theta = 2°$, for each frequency.

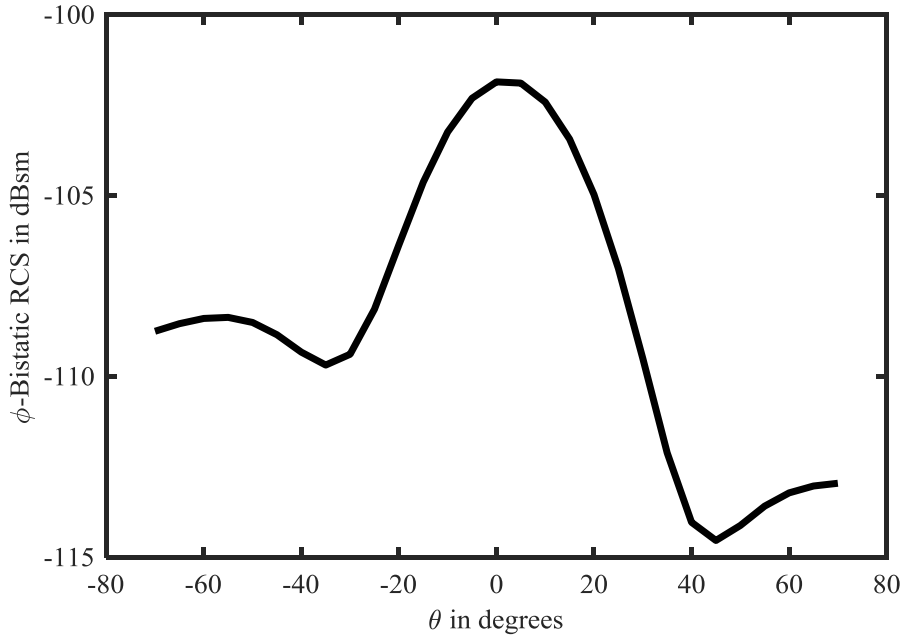

Figure 32. Bistatic response of 1.5λ aluminum design at 30 THz from excitation at θ=20° and ϕ=90°.

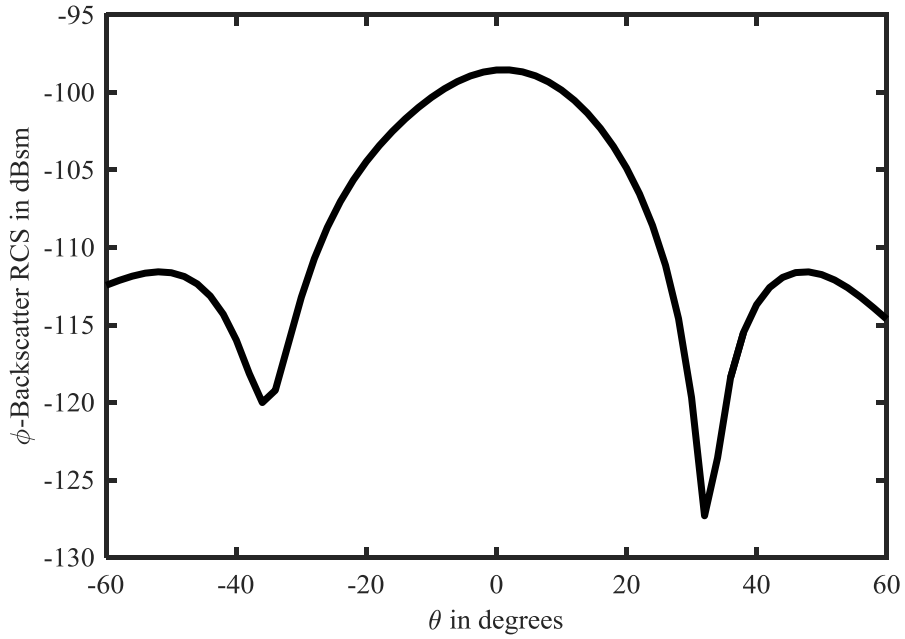

Figure 33. Monostatic response of 1.5λ aluminum design showing approximately 35° retrodirective beamwidth with ϕ set at 90°.

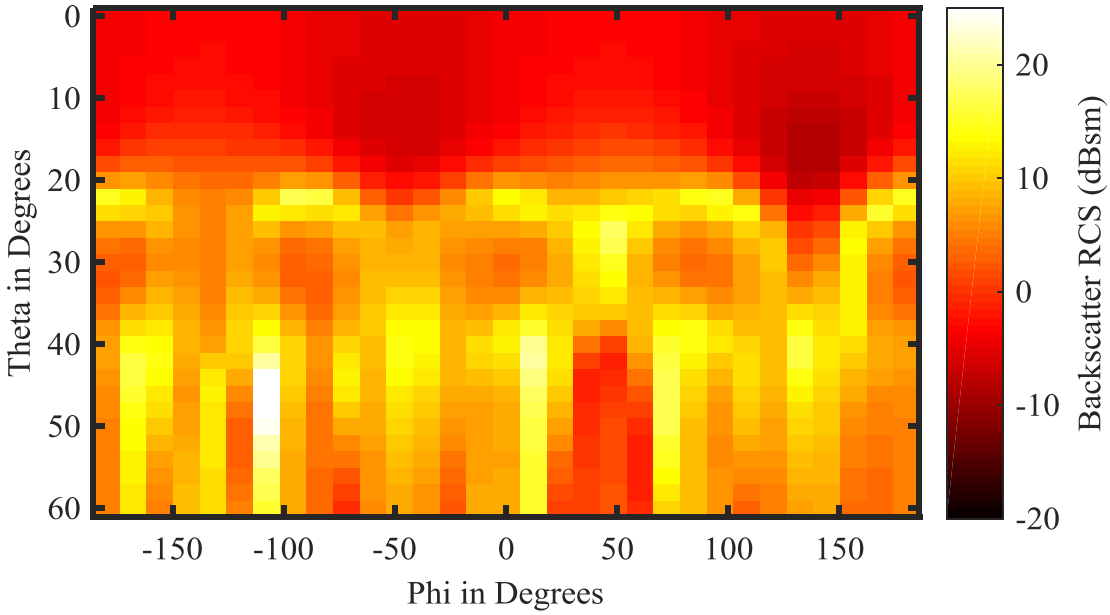

Figure 34. The aluminum design normalized backscatter with short exterior traces at 30 THz excited at ϕ values from $-180°$ to $180°$ with $\Delta\phi = 12°$, θ values from $0°$ to $60°$ with $\Delta\theta = 2°$.

Summary

The results from the convergence tests show that the HPC solutions are at worst under predicting the backscatter values. The comparison of the normalized linear RCS ratio gives a good comparison for performance, shown in Table 7, and shows using hafnium oxide as a substrate material gives overall broadband performance in the IR band of 8-12 μm better than the performance seen in the 2GHz design over a similar range of frequencies. The aluminum design performed very close to the same as the gold design, so its cost and bonding advantages making it the better choice.

Table 7. Linear RCS Ratio of simulated designs

Design	Linear RCS Ratio	Performance Factor
Christodoulou and Chrissoulidis design	119.26	1.00
Modified design with PEC traces	124.18	1.04
Modified design w/o transformers	127.88	1.07
Germanium substrate with PEC traces	47.50	0.40
Hafnium Oxide with PEC traces(2.5λ)	514.25	4.31
Hafnium Oxide with PEC traces(1.5λ)	246.05	2.06
Gold on hafnium substrate(2.5λ)	391.07	3.28
Gold on hafnium substrate(1.5λ)	432.00	3.62
Aluminum on hafnium substrate(2.5λ)	385.63	3.23
Aluminum on hafnium substrate(1.5λ)	423.16	3.55

V. Conclusions and Recommendations

Chapter Overview

This chapter presents the conclusions and significance of the research performed. Recommendations for future work are presented and the overall results summarized.

Conclusions of Research

The results of this research show that it is possible to implement the Van Atta array to be effective in the long-wave-IR range of the EM spectrum centered on $30\,\text{THz}$. The results of the simulations show that both gold and aluminum are effective metals to use in the design. The hafnium oxide is the better choice, over germanium, as a dielectric substrate material, providing better broadband performance, patch coverage, and impedance matching between the patches and transmission traces. The design will require X-ray or E-beam lithography for implementation.

Significance of Research

An improved method of controlling the noise signal in IR detectors will improve the performance and efficiency of detectors. Better IR detection using uncooled systems will allow uncooled systems use in applications normally needing higher-cost cooled systems. Being able to use less expensive systems will also reduce the cost of IR detection methods employed in the field and the lab. This work examined the suitability of one such method, and indicated potential sufficient to justify further investigation.

Recommendations for Future Research

The approximate equation used to find the required substrate height is based on typical RF frequencies for broadband performance. Modification of the design to incorporate different substrate heights and comparing the performance would lead to better understanding of how the substrate height affects performance in the IR portion of the EM spectrum.

Implementing the design in FLO-K to analyze the performance of an array of the design is a necessary step toward determining if the design is capable of being used as a coating in optical train application. Using FLO-K to process array simulations will allow a determination to be made, as to whether the design will meet application specific goals when arranged in as an array of arrays. Creating a physical example of the design and testing real world performance will validate the SENTRi/FLO-K simulation results.

Summary

Using HPC resources and the CREATE-RF series of software tools shows that, using hafnium oxide as a substrate material, a viable Van Atta array can be created that operates in the long-wave-IR range of the EM spectrum of $8-12\mu m$. Also demonstrated is that gold and aluminum perform well in simulation. The lower cost and improved oxide bonding characteristics of aluminum may reasonably be taken to balance its slightly lower retrodirective scattering performance relative to gold. Future work could involve investigating the limitations of microfabrication of the design or the implementation of the design in an array to show the performance as an engineered surface.

Appendix A

The research concentrated on the overall broadband backscatter RCS response to compare performance, however it is worth noting that frequency response variations changes with each modification. Figure 35 shows the frequency response of the GHz designs by plotting the average RCS at each measured frequency. Table 8 shows that both the initial design and first modified design actually peak at 1.9743 GHz instead of the designed 2 GHz. The difference could come from the PEC assumptions or some difference in the way modeling or simulations were done. Since Christodoulou and Chrissoulidis [3] did not publish any results other than 2 GHz measurements it is unknown if their design would measure a peak performance different than 2 GHz. When the design is further modified to remove the transformers the peak performance shifts to 1.9467 GHz. Figure 35 shows that even though the peak of the design without transformers is lower than the other 2 GHz design peaks the other peaks that appear without the transformers allow an overall better RCS performance.

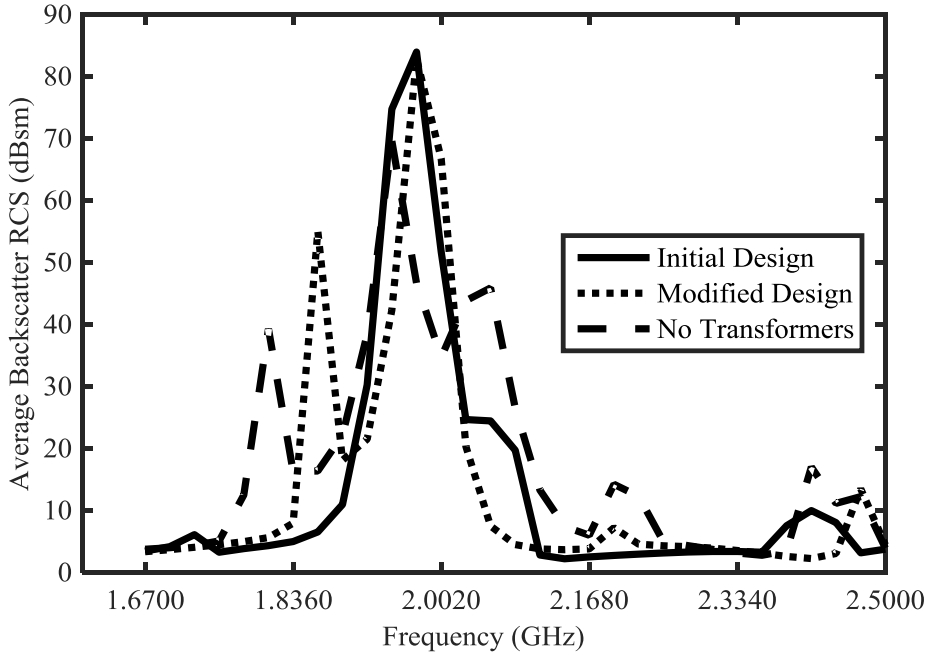

Figure 35. The frequency response of backscatter RCS in the GHz designs shows the peak performance occurs at 1.9743 GHz for the published design and first modification, but the performance peak shifts to 1.9467 GHz with the removal of the quarter wave transformers.

Table 8. Peak Frequency showing highest average backscatter RCS

Design	Freq
Initial	1.9743 GHz
Modified	1.9743 GHz
No Transformers	1.9467 GHz
Germanium	36.6667 THz
Hafnium Oxide	31.6667 THz
Gold on Hafnium (2.5λ)	30.8333 THz
Aluminum on Hafnium Substrate (2.5λ)	33.3333 THz
Gold on Hafnium (1.5λ)	32.5000 THz
Aluminum on Hafnium Substrate (1.5λ)	32.5000 THz

Figure 36 shows that performance of the hafnium oxide substrate is consistently higher than the germanium substrate design with distinctive peaks in the response. While Table 8 shows that germanium peaks at 36.6667 THz and the hafnium design peaks at 31.6667 THz.

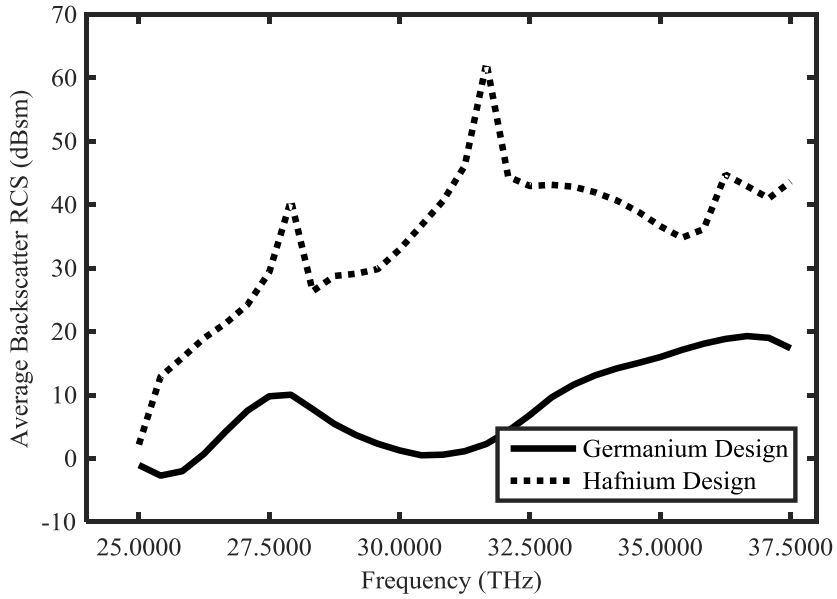

Figure 36. The frequency response of backscatter RCS in the THz substrate designs shows that the hafnium oxide design has consistently higher performance than the germanium design with a peak at 31.6667 THz, which is fairly close to the designed center frequency of 30 THz.

Figure 37 and Figure 38 show how close in performance the gold and aluminum designs behave. Table 8 shows that the $2.5\lambda_g$ gold design peaks at 30.8333 THz, which is very close to the designed center frequency of 30 THz. The $2.5\lambda_g$ aluminum design peaks at 33.333 THz but Figure 37 demonstrates that the 30.8333 THz peak is very close as well. Figure 38 and Table 8 show that both of the $1.5\lambda_g$ designs peak at 32.5 THz with higher peaks than the $2.5\lambda_g$ designs, indicating that overall performance might be improved with some further design refinement to better center the performance around 30 THz.

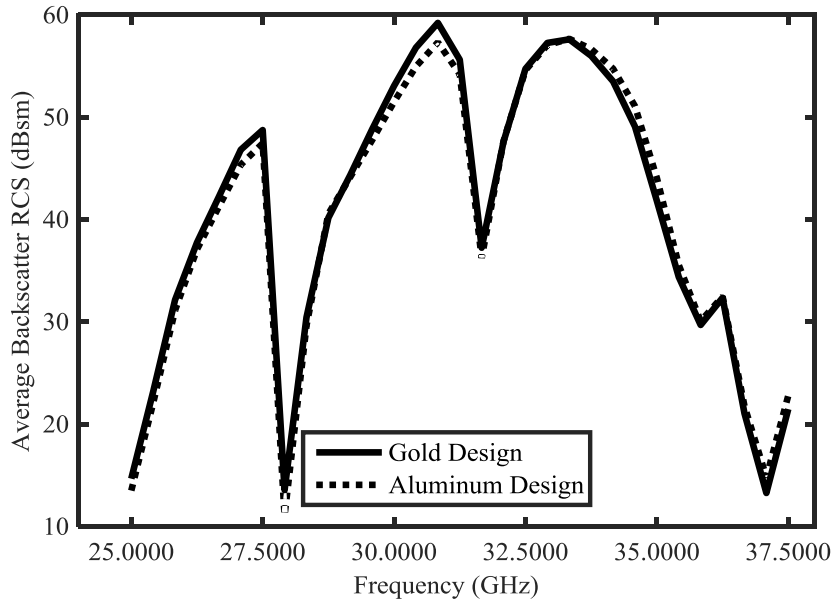

Figure 37. The frequency response of backscatter RCS in the metal designs with 2.5λ trace length differences show major peaks at 30.8333 THz and 33.3333 THz.

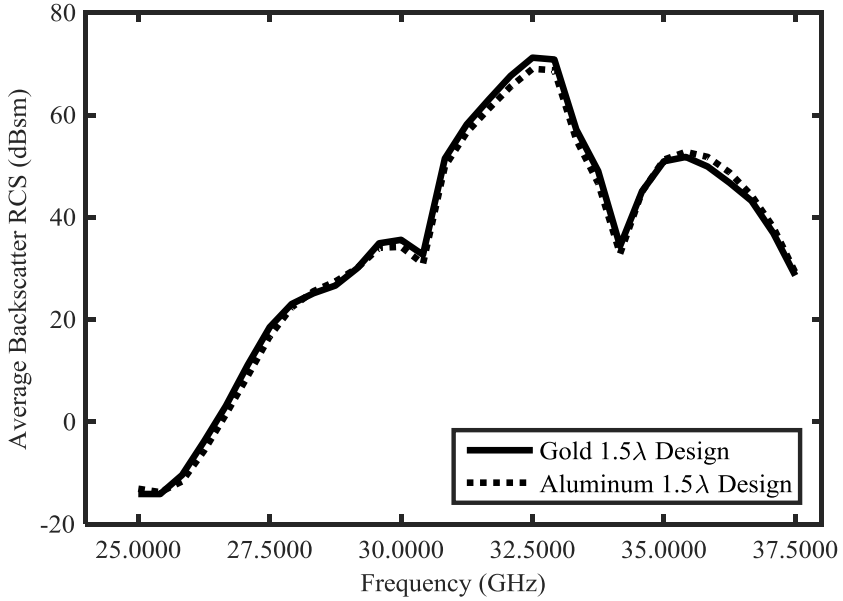

Figure 38. The frequency response of backscatter RCS in the metal designs with 1.5λ trace length differences show the peak performance at 32.5 THz and at an overall higher RCS on average than the shorter traces.

Bibliography

[1] B. Nair and V. F. Fusco, "Two-dimensional planar passive retrodirective array," *Electron. Lett.*, vol. 39, no. 10, pp. 768–769, 2003.

[2] E. Sharp and M. Diab, "Van Atta reflector array," *IRE Trans. Antennas Propag.*, vol. 8, no. 4, pp. 1951–1953, 1960.

[3] M. G. Christodoulou and D. P. Chrissoulidis, "2D Van Atta retrodirective array using dual polarized two-port square microstrip patches," in *Antennas and Propagation, 2001. Eleventh International Conference on (IEE Conf. Publ. No. 480)*, 2001, vol. 2, pp. 814–816.

[4] T. J. Bright, J. I. Watjen, Z. M. Zhang, C. Muratore, and A. A. Voevodin, "Optical properties of HfO2 thin films deposited by magnetron sputtering: From the visible to the far-infrared," *Thin Solid Films*, vol. 520, no. 22, pp. 6793–6802, 2012.

[5] S. N. Mcconnell, "Spectral and spatial coherent emission of thermal radiation from metal-semiconductor nanostructures," Air Force Institute of Technology, 2012.

[6] C. a Balanis, *Modern Antenna Handbook*. 2008.

[7] S. Franssila, *Introduction to Microfabrication*, 2nd ed. Wiley, 2010.

[8] T. Edwards, *Foundations for microstrip circuit design*. J. Wiley, 1981.

[9] HPCMP/CREATE-MG, "Capstone user manual." 2015.

[10] HPCMP/CREATE-RF, "SENTRi 5.0 User manual." 2015.

[11] R. Hartley, *RF / Microwave PC Board Design and Layout*, vol. 4. .

[12] Y. C. Guo, X. W. Shi, and L. Chen, "Retrodirective array technology Y. C. Guo, X. W. Shi, and L. Chen," vol. 5, pp. 153–167, 2008.

[13] B. E. Bernacki, N. C. Anheier, K. Krishnaswami, B. D. Cannon, and K. B. Binkley, "Design and fabrication of efficient miniature retroreflectors for the mid- and long-range infrared," *Proc. SPIE*, vol. 6940. p. 69400X–69400X–11, 2008.

[14] L. C. Van Atta, "Electromagnetic Reflector," Patent # 2908002, Serial No. 514040.

[15] K. S. B. Yau, "Development of a passive retrodirective Van Atta array reflector at X-band," in *International Conference on Radar*, 2013.

[16] S.-J. Chung, S.-M. Chen, and Y.-C. Lee, "A novel bi-directional amplifier with applications in active Van Atta retrodirective arrays," *Microw. Theory Tech. IEEE Trans.*, vol. 51, pp. 542–547, 2003.

[17] K. Carver and J. Mink, "Microstrip antenna technology," *IEEE Trans. Antennas Propag.*, vol. 29, no. 1, pp. 2–24, 1981.

[18] C. A. Balanis, *Advanced Engineering Electromagnetics*, 2nd ed. Wiley, 2012.

[19] D. M. Dobkin, *The RF in RFID: UHF RFID in Practice*. Newnes, 2012.

[20] H. A. Macleod, "Structure-related optical properties of thin films," *J. Vac. Sci. Technol. A Vacuum, Surfaces, Film.*, vol. 4, no. 3, p. 418, May 1986.

[21] D. E. Aspnes, "Optical properties of thin films," *Thin Solid Films*, vol. 89, no. 3, pp. 249–262, Mar. 1982.

[22] A. N. Broers, "The Clifford Paterson Lecture, 1986. Limits of Thin-Film Microfabrication," *Proc. R. Soc. London A Math. Phys. Eng. Sci.*, vol. 416, no. 1850, pp. 1–42, Mar. 1988.

[23] Nanoscribe-GmbH, "Nanoscribe sales flyer," Nanoscribe of Germany, 2013.

[24] W. Wu, Z. Yu, S. Y. Wang, R. S. Williams, Y. Liu, C. Sun, X. Zhang, E. Kim, Y. R. Shen, and N. X. Fang, "Midinfrared metamaterials fabricated by nanoimprint lithography," *Appl. Phys. Lett.*, vol. 90, no. 6, pp. 14–16, 2007.

[25] F. Capolino, *Applications of Metamaterials*. CRC Press, 2009.

[26] C. M. Soukoulis, M. Kafesaki, and E. N. Economou, "Negative-index materials: New frontiers in optics," *Adv. Mater.*, vol. 18, no. 15, pp. 1941–1952, 2006.

[27] C. M. Soukoulis, J. Zhou, T. Koschny, M. Kafesaki, and E. N. Economou, "The science of negative index materials," *J. Phys. Condens. Matter*, vol. 20, no. 30, p. 304217, 2008.

[28] C. M. Soukoulis, S. Linden, and M. Wegener, "Negative Refractive Index at," *Science (80-.).*, vol. 315, no. January, pp. 47–50, 2007.

[29] P. B. K. C. Gupta, R. Garg, I. Bahl, *Microstrip lines and slotlines*, 2nd ed. Artch House, 1996.

[30] J. Howell, "Microstrip antennas," *Antennas Propagation, IEEE Trans.*, vol. 23, no. 1, pp. 90–93, 1975.

[31] AFRL/RX, "As measured infrared variable angle spectroscopic ellipsometry (IR-VASE)." .

[32] P. Collins, "Lecture notes EENG627 AFIT." 2015.

REPORT DOCUMENTATION PAGE

Form Approved
OMB No. 074-0188

PLEASE DO NOT RETURN YOUR FORM TO THE ABOVE ADDRESS.

1. REPORT DATE *(DD-MM-YYYY)*	2. REPORT TYPE	3. DATES COVERED *(From – To)*
24-03-2016	Master's Thesis	Oct 2014 –Mar 2016

4. TITLE AND SUBTITLE
Design and Analysis of a Retroreflective Array for IR Application

5a. CONTRACT NUMBER

5b. GRANT NUMBER

5c. PROGRAM ELEMENT NUMBER

6. AUTHOR(S)
Bollinger, Michael E., Capt, USAF

5d. PROJECT NUMBER
N/A

5e. TASK NUMBER

5f. WORK UNIT NUMBER

7. PERFORMING ORGANIZATION NAMES(S) AND ADDRESS(S)
Air Force Institute of Technology
Graduate School of Engineering and Management (AFIT/EN)
2950 Hobson Way, Building 640
WPAFB OH 45433-8865

8. PERFORMING ORGANIZATION REPORT NUMBER
AFIT-ENG-MS-16-M-005

9. SPONSORING/MONITORING AGENCY NAME(S) AND ADDRESS(ES)
Intentionally Left Blank

10. SPONSOR/MONITOR'S ACRONYM(S)

11. SPONSOR/MONITOR'S REPORT NUMBER(S)

12. DISTRIBUTION/AVAILABILITY STATEMENT
DISTRIBUTION STATEMENT A: APPROVED FOR PUBLIC RELEASE; DISTRIBUTION UNLIMITED

13. SUPPLEMENTARY NOTES
This material is declared a work of the U.S. Government and is not subject to copyright protection in the United States.

14. ABSTRACT

This research investigates the adaptation of a Van Atta style of retrodirective array designed to work at 2 GHz to work in the infrared spectrum of 8-12 μm centered at 30 THz. The Computational Research and Engineering Acquisition Tools and Environments (CREATE) software suite and high performance computing (HPC) resources of the HPC Modernization program were utilized to model and simulate multiple steps of an adaptation process to illustrate and examine the incremental performance changes of frequency scaling the design. Two different substrate materials, germanium and hafnium oxide, are evaluated as the dielectric materials, and a comparison of the broadband performance of scaled designs using both dielectric materials shows that hafnium oxide provides better performance than germanium for this application. In addition, both gold and aluminum are evaluated for use in scaled designs. The results suggest that the cost savings and oxide bonding benefits of aluminum outweigh the slight performance advantage of gold. The Van Atta array concept is adaptable to IR wavelengths and microfabrication. Improved final broadband performance of the scaled design is a factor of approximately three and a half better than the 2 GHz design.

15. SUBJECT TERMS
Retrodirective, Van Atta Array, Long-wave-IR

16. SECURITY CLASSIFICATION OF:			17. LIMITATION OF ABSTRACT	18. NUMBER OF PAGES	19a. NAME OF RESPONSIBLE PERSON
a. REPORT	b. ABSTRACT	c. THIS PAGE			Maj. Michael D. Seal (ENG)
U	U	U	UU	79	19b. TELEPHONE NUMBER *(Include area code)* (937) 255-3636, x 3369 (michael.seal@afit.edu)

Standard Form 298 (Rev. 8-98)
Prescribed by ANSI Std. Z39-18